

Effects of finite-rate chemistry and detailed transport on the instability of jet diffusion flames

Yee Chee See and Matthias Ihme[†]

Department of Mechanical Engineering, Stanford University, Stanford, CA 94305, USA

(Received 25 March 2013; revised 7 February 2014; accepted 15 February 2014)

Local linear stability analysis has been shown to provide valuable information about the response of jet diffusion flames to flow-field perturbations. However, this analysis commonly relies on several modelling assumptions about the mean flow prescription, the thermo-viscous-diffusive transport properties, and the complexity and representation of the chemical reaction mechanisms. In this work, the effects of these modelling assumptions on the stability behaviour of a jet diffusion flame are systematically investigated. A flamelet formulation is combined with linear stability theory to fully account for the effects of complex transport properties and the detailed reaction chemistry on the perturbation dynamics. The model is applied to a methane-air jet diffusion flame that was experimentally investigated by Füri *et al.* (*Proc. Combust. Inst.*, vol. 29, 2002, pp. 1653–1661). Detailed simulations are performed to obtain mean flow quantities, about which the stability analysis is performed. Simulation results show that the growth rate of the inviscid instability mode is insensitive to the representation of the transport properties at low frequencies, and exhibits a stronger dependence on the mean flow representation. The effects of the complexity of the reaction chemistry on the stability behaviour are investigated in the context of an adiabatic jet flame configuration. Comparisons with a detailed chemical-kinetics model show that the use of a one-step chemistry representation in combination with a simplified viscous-diffusive transport model can affect the mean flow representation and heat release location, thereby modifying the instability behaviour. This is attributed to the shift in the flame structure predicted by the one-step chemistry model, and is further exacerbated by the representation of the transport properties. A pinch-point analysis is performed to investigate the stability behaviour; it is shown that the shear-layer instability is convectively unstable, while the outer buoyancy-driven instability mode transitions from absolutely to convectively unstable in the nozzle near field, and this transition point is dependent on the Froude number.

Key words: absolute/convective instability, combustion, laminar reacting flows

1. Introduction

Combustion technologies for aviation and transportation systems typically utilize non-premixed combustion strategies. In these systems, heat release and fuel conversion rely on the rapid mixing between fuel and oxidizer. With the increasing interest in

[†]Email address for correspondence: mihme@stanford.edu

developing compact combustion systems, having higher power output and energy densities, more effective mixing strategies become necessary. Thermo-diffusive and hydrodynamic instabilities can potentially assist in improving the mixing rate by altering the flame dynamics and promoting transition from laminar to turbulent combustion regimes.

Instabilities in laminar diffusion flames have been investigated experimentally, theoretically and computationally, and the review article by Matalon (2007) provides a comprehensive overview on this subject. Early investigations considered buoyancy-driven instabilities in the context of flame flickering (Chamberlin & Rose 1948; Chen *et al.* 1989; Maxworthy 1999), and Mie scattering and photographic imaging provided details about the vortical structure in the inner and outer regions of the flame. Buckmaster & Peters (1988) performed linear stability analysis and identified the most unstable modified Kelvin–Helmholtz mode at a frequency of 17 Hz. This result is in agreement with experiments by Chen *et al.* (1989), which is remarkable considering that this analysis was performed at an arbitrary downstream location while neglecting viscous and buoyancy effects in their stability analysis.

Because of its geometric simplicity, considerable work has been conducted on the computational analysis of instabilities in reacting shear layers. The work by Shin & Ferziger (1991) identified three distinct instability modes that are associated with an inner mode in the middle of the shear layer and two outer modes in the fuel and oxidizer streams. By performing an inviscid instability analysis, they showed that the heat release suppresses the central hydrodynamic mode and amplifies the outer modes. This work was complemented by comprehensive parametric investigations by Day, Reynolds & Mansour (1998) to elucidate how the effects of compressibility, density and velocity ratios, and heat release affect these instability modes. Their calculations showed that compressibility, heat release and fuel/oxidizer density ratio are more relevant in affecting the flow structure than the stoichiometry and velocity differences between the two streams.

The characteristics of the flow instability can be further elucidated by examining the impulse response of the linear system (Huerre & Monkewitz 1990). If the perturbations are amplified, the flow can be categorized as convectively unstable or absolutely unstable, and Briggs' method can be used to distinguish among the two regimes (Briggs 1964). Perturbations in a convectively unstable flow will propagate unidirectionally, while perturbations in the absolutely unstable regime will fully contaminate the flow. Therefore, an absolutely unstable flow can oscillate even without the continuous presence of external perturbations, and a buoyantly driven jet flame is a classical example for this (Chen *et al.* 1989; Katta & Roquemore 1993; Lingens *et al.* 1996; Juniper, Li & Nichols 2009).

In order to make the instability analysis of chemically reacting flows accessible to theoretical investigations, different levels of model approximations associated with (i) velocity field, (ii) thermo-viscous-diffusive transport and (iii) reaction chemistry are commonly employed. In particular, the mean flow is typically represented using analytical profiles, in which the shear-layer thickness and other describing parameters are adjusted to obtain agreement with measurements. Often, the effects of viscosity are neglected in the stability analysis, and only the inviscid stability problem is considered (Buckmaster & Peters 1988; Day *et al.* 1998). More detailed investigations introduce viscous contributions by approximating the transport properties either as constant or as linearly dependent on temperature. The latter assumption is referred to as the Chapman approximation. In addition, the description of the reaction chemistry is usually limited to a one-step chemical model, which provides only an incomplete

description of the structure of non-premixed flames (Williams 1991). Owing to the limitation of these chemical models, rate coefficients and other parameters are often adjusted to match experimental data. Despite these simplifications, the results obtained from these investigations can explain mechanisms that characterize the stability behaviour (Lingens *et al.* 1996; Füri 2001; Füri *et al.* 2002). However, it is currently not clear how these modelling assumptions affect the results and conclusions drawn from these stability investigations. While this fundamental question has not been answered for chemically reacting flows, progress has been made on examining the effects of the parametric representation of the mean flow (velocity and density) and transport properties on the stability in heated jets. Theoretical investigations suggest that the jet can become absolutely unstable if the density ratio is smaller than a critical value (Monkewitz & Sohn 1988). The effects of the base flow on the growth rate in these jet flows has been investigated by different groups (Nichols, Schmid & Riley 2007; Coenen, Sevilla & Sánchez 2008; Srinivasan, Hallberg & Strykowski 2010; Lesshafft & Marquet 2010; Coenen & Sevilla 2012), showing that critical transition conditions and the absolute growth rate depend on the base-flow profiles, density ratio, momentum thickness and the proximity of the inflection points for density and velocity.

The objective of this work is to extend previous analysis in inert jets to chemically reacting jets by systematically examining the effects of the description of mean flow profiles, the functional dependence of constitutive relations on temperature and species composition, and the representation of the reaction chemistry on this instability behaviour. To this end, a local linear stability method is developed in which a flamelet formulation is used to account for the effects of complex transport properties and the detailed reaction chemistry on the perturbation dynamics. Consistent with the stability analysis, the base flow is obtained from a detailed simulation, containing the same level of physical representation. This eliminates the explicit dependence on prescribed mean flow profiles and model parameters. The mathematical model is presented in § 2. The model is applied to a jet diffusion flame configuration that was experimentally investigated by Füri *et al.* (2002), and the burner configuration is discussed in § 3. Following a comparison of modelling results with experimental data and linear stability results, which is presented in § 4.1, a sensitivity investigation is performed by considering the effects of the mean flow representation (analytic and realistic flow-field representation), the description of thermodynamic transport properties (calorically perfect mixture and ideal gas model), viscous-diffusive transport (Chapman approximation and mixture-averaged transport), and the reaction chemistry (global one-step chemistry and detailed chemistry model consisting of 279 reactions among 49 species) on the instability behaviour. The results from these investigations are presented in § 4.2, in which the convective/absolute perturbation dynamics of the inner Kelvin–Helmholtz-type instability mode and the outer buoyancy-driven mode are examined. This section is followed by a discussion of the nonlinear instability behaviour using Fourier analysis and proper orthogonal decomposition to analyse the coupling between the inner and outer modes and to identify energetically coherent structures. The paper finishes with conclusions.

2. Mathematical model

2.1. Governing equations

The instantaneous governing equations, describing conservation of mass, momentum, mixture fraction and progress variable, are solved in the low-Mach-number limit

(Kreiss, Lorenz & Naughton 1991; Müller 1999). In this approximation, acoustic effects and variations in thermochemical composition with respect to pressure perturbations are neglected. The resulting conservation equations can then be written in dimensionless form as:

$$\partial_t \rho + \nabla \cdot (\rho \mathbf{u}) = 0, \quad (2.1a)$$

$$\partial_t(\rho \mathbf{u}) + \nabla \cdot (\rho \mathbf{u} \otimes \mathbf{u}) = -\nabla p + \frac{1}{Re} \nabla \cdot \boldsymbol{\tau} - \frac{1}{Fr^2} \rho \hat{\mathbf{j}}, \quad (2.1b)$$

$$\partial_t(\rho Z) + \nabla \cdot (\rho \mathbf{u} Z) = \frac{1}{Re Sc} \nabla \cdot (\nu \nabla Z), \quad (2.1c)$$

$$\partial_t(\rho C) + \nabla \cdot (\rho \mathbf{u} C) = \frac{1}{Re Sc} \nabla \cdot (\nu \nabla C) + Da \dot{\omega}_C, \quad (2.1d)$$

where t is the time, $\mathbf{x} = (x, r, \theta)^T$ is the spatial coordinate vector in cylindrical form, $\mathbf{u} = (u, v, w)^T$ is the velocity vector, ρ is the density, p is the hydrodynamic pressure, Z is the mixture fraction, C is the reaction progress variable and $\dot{\omega}_C$ is the production rate. The viscous stress tensor is denoted by $\boldsymbol{\tau}$, $\hat{\mathbf{j}}$ is the unit vector pointing in the direction of gravity, ν is the species diffusivity and μ is the dynamic viscosity. All variables in (2.1) are non-dimensionalized with the burner exit diameter D_0 , jet exit velocity U_0 and thermo-viscous properties in the ambient air stream. (See § 3 for numerical values of all reference quantities.) All reference quantities are denoted by a subscript ‘0’. The dimensional groups that are defined in this work are the Reynolds number Re , the Schmidt number Sc , the Damköhler number Da and the Froude number Fr , having the following definitions:

$$Re = \frac{\rho_0 U_0 D_0}{\mu_0}, \quad Sc = \frac{\mu_0}{\nu_0}, \quad Da = \frac{D_0}{U_0} \frac{\dot{\omega}_{C,st}^*}{\rho_0 C_{st}^*}, \quad Fr = \frac{U_0}{\sqrt{g D_0}}. \quad (2.2)$$

The chemical time scale, appearing in the definition of the Damköhler number, is defined from the stoichiometric value of the progress variable, C_{st}^* , evaluated at its maximum production rate $\dot{\omega}_{C,st}^*$.

Equations (2.1) can formally be written in operator form as

$$\mathcal{M}(\phi, \xi)\phi = 0, \quad (2.3)$$

in which the vectors of state variables, ϕ , and constitutive relations, ξ , have the following definitions:

$$\phi = (\mathbf{u}, p, Z, C)^T, \quad (2.4a)$$

$$\xi = (\rho, \mu, \nu, \dot{\omega}_C)^T. \quad (2.4b)$$

Note that the state vector is a function of the space-time coordinate, $\phi(t, \mathbf{x})$, while all constitutive relations can be expressed solely in terms of Z and C , namely $\xi(Z, C)$. The vector of constitutive relations is evaluated from a flamelet formulation, which is presented in the next section.

2.2. Flamelet formulation and flamelet/progress variable model

In the following, a local linear stability analysis of a jet diffusion flame is performed. This analysis utilizes a flamelet-based combustion model to account for detailed

reaction chemistry, complex viscous-diffusive transport and temperature-dependent thermal properties. The underlying assumption of the flamelet formulation is the consideration of a diffusion flame as an ensemble of laminar one-dimensional flame structures (Peters 1983, 1984). At sufficiently large Damköhler number or sufficiently high activation energy, chemical reactions and heat transfer are confined to a thin reaction–diffusion layer. The surrounding flow field is only able to deform and stretch the flame but is unable to penetrate and destroy the reaction zone.

The structure of these so-called flamelets is represented by the flamelet equations, which can be derived by introducing a new coordinate system that is locally attached to the surface of the stoichiometric mixture. By associating the distance normal to the flame surface with the mixture fraction Z following a Crocco-type transformation and neglecting higher-order terms, the one-dimensional steady laminar flamelet equations for unity-Lewis-number flames can be written as (Peters 1984):

$$-\rho \frac{\chi_Z}{2} \frac{\partial^2 \mathbf{Y}}{\partial Z^2} = Re Sc Da \dot{\boldsymbol{\omega}}, \quad (2.5a)$$

$$-\rho \frac{\chi_Z}{2} \frac{\partial^2 T}{\partial Z^2} - \rho \frac{\chi_Z}{2 \langle c_p \rangle} \left(\mathbf{c}_p \cdot \frac{\partial \mathbf{Y}}{\partial Z} + \frac{\partial \langle c_p \rangle}{\partial Z} \right) \frac{\partial T}{\partial Z} = Re Sc Da Ce \frac{1}{\langle c_p \rangle} \dot{\omega}_T. \quad (2.5b)$$

Here \mathbf{Y} is the mass-fraction vector of N_S chemical species, T is the temperature, \mathbf{c}_p is the vector of specific heats at constant pressure for all species, and $\langle c_p \rangle = \mathbf{c}_p \cdot \mathbf{Y}$ is the specific heat of the mixture. The density appearing in (2.5) is obtained from the state equation, $p = \rho RT$, considering a constant thermodynamic pressure. The production rate of all species is denoted by the vector $\dot{\boldsymbol{\omega}}$, $\dot{\omega}_T$ is the heat release rate, and the negative heat release parameter $Ce = h_{C,0}/(c_{p,0}T_0)$ compares the chemical and sensible enthalpies. The scalar dissipation rate is defined as $\chi_Z = 2\nu/\rho|\nabla Z|^2$.

Although the present investigation is concerned with methane flames, for which preferential diffusion effects are small, the flamelet formulation has been extended to account for the effects of non-unity Lewis number (Pitsch & Peters 1998), radiation or flame curvature (Kortschik, Honnet & Peters 2005). With this, the flamelet-based stability method that is developed in this work can also be extended to study physically more complex combustion systems, such as hydrogen flames (Katta, Goss & Roquemore 1994), cellular and thermo-diffusive instabilities near extinction (Füri, Papas & Monkewitz 2000; Lo Jacono & Monkewitz 2007), or radiation-induced instabilities and edge-flame stabilization (Kurdyumov & Matalon 2002; Nichols & Schmid 2008).

The solution of (2.5) can be parametrized by a two-dimensional manifold. To this end, a flamelet/progress variable (FPV) model (Pierce & Moin 2004; Ihme, Cha & Pitsch 2005) is introduced, in which mixture fraction Z and reaction progress variable C are used to parametrize this flamelet manifold,

$$\boldsymbol{\psi} = \mathcal{F}_{\psi}(Z, C), \quad (2.6)$$

where $\boldsymbol{\psi} = (\mathbf{Y}, T, \dot{\boldsymbol{\omega}}, \dot{\omega}_T, \rho, \nu, \mu)^T$ is the vector of all thermochemical variables, \mathcal{F}_{ψ} denotes the FPV library, and the reaction progress variable is defined as $C = Y_{CO_2} + Y_{CO} + Y_{H_2O} + Y_{H_2}$ (Ihme, Shunn & Zhang 2012). This FPV library is precomputed prior to the simulation and the linear stability analysis. All thermochemical quantities ξ that appear in (2.1) are then directly retrieved from this library during the simulation.

2.3. Linear stability analysis

In the local linear stability analysis, the state variables in (2.1) are decomposed into a mean flow and a perturbation field:

$$\boldsymbol{\phi}(t, \mathbf{x}) = \bar{\boldsymbol{\phi}}(\mathbf{x}) + \boldsymbol{\phi}'(t, \mathbf{x}). \quad (2.7)$$

Here and in the following, mean quantities $\bar{\boldsymbol{\phi}}$ are prescribed from analytic profiles or by averaging the detailed simulation results in time.

In chemically reacting flows, the constitutive state vector ξ , defined in (2.4b), is nonlinearly dependent on the chemical composition and the temperature. To account for these nonlinearities in the stability analysis, the FPV formulation is utilized, and all constitutive quantities are expanded locally around the mean mixture fraction \bar{Z} and mean reaction progress variable \bar{C} . This can be written as

$$\xi = \bar{\xi} + \xi', \quad (2.8a)$$

$$= \mathcal{F}_\xi(\bar{Z}, \bar{C}) + \left(\frac{\partial \mathcal{F}_\xi}{\partial Z} \Big|_{\bar{Z}, \bar{C}} Z' + \frac{\partial \mathcal{F}_\xi}{\partial C} \Big|_{\bar{Z}, \bar{C}} C' \right), \quad (2.8b)$$

in which the expressions $\partial_Z \mathcal{F}_\xi$ and $\partial_C \mathcal{F}_\xi$ are directly evaluated by differentiating the FPV flamelet library (2.6). Upon introducing this flamelet expression into (2.1) and neglecting higher-order terms, the linearized form of the governing equations can be formally written as

$$\mathcal{N}(\bar{\boldsymbol{\phi}}, \xi') \boldsymbol{\phi}' = 0, \quad (2.9)$$

where \mathcal{N} is the linearized perturbation operator.

After introducing the normal mode decomposition,

$$\boldsymbol{\phi}' = \hat{\boldsymbol{\phi}}(r) \exp\{i(\alpha x + m\theta - \omega t)\}, \quad (2.10)$$

into (2.9), the resulting equations are dependent on the frequency $\omega = \omega_r + i\omega_i$, the axial wavenumber $\alpha = \alpha_r + i\alpha_i$ and the azimuthal mode number m . In the following, a spatial stability analysis is performed, and the complex-valued wavenumbers are evaluated by solving the equations for a given real-valued ω_r . The resulting spatial eigenvalue problem can be written as

$$\mathbf{A}\hat{\boldsymbol{\phi}} = i\alpha \mathbf{B}\hat{\boldsymbol{\phi}}, \quad (2.11)$$

where the eigenfunction vector $\hat{\boldsymbol{\phi}}$ is defined as

$$\hat{\boldsymbol{\phi}} = (\hat{u}, \hat{u}_x, \hat{v}, \hat{v}_x, \hat{w}, \hat{w}_x, \hat{p}, \hat{Z}, \hat{Z}_x, \hat{C}, \hat{C}_x)^T, \quad (2.12)$$

and the coefficient matrices \mathbf{A} and \mathbf{B} are given in appendix A.

In this analysis, the most unstable axisymmetric instability mode with $m = 0$ is considered. For this case, the boundary conditions imposed on the perturbation vector are

$$r=0: \quad \frac{d\hat{u}}{dr} = 0, \quad \hat{v} = 0, \quad \hat{w} = 0, \quad \frac{d\hat{p}}{dr} = 0, \quad \frac{d\hat{Z}}{dr} = 0, \quad \frac{d\hat{C}}{dr} = 0, \quad (2.13)$$

$$r \rightarrow \infty: \quad \hat{u} = 0, \quad \hat{v} = 0, \quad \hat{w} = 0, \quad \hat{p} = 0, \quad \hat{Z} = 0, \quad \hat{C} = 0. \quad (2.14)$$

The general eigenvalue problem, equation (2.11), is discretized using a collocation method (Schmid & Henningson 2001). In this method, the disturbance vector $\hat{\boldsymbol{\phi}}$ is expanded in polynomial space, and the discretized system is solved using an Arnoldi method.

2.4. Evaluation of convective and absolute instability modes

Briggs' method is commonly employed to determine if an instability is convective or absolute in nature (Briggs 1964). This method considers the structure and value of ω_i at the saddle point in the complex α -plane, i.e.

$$\frac{\partial \omega}{\partial \alpha} = 0. \quad (2.15)$$

In the case that one or more saddle points are located in the lower complex frequency plane, $\omega_i < 0$, the instability is convective. A necessary criterion for an absolute instability is that the saddle point is in the upper complex frequency plane. The second criterion is that the same saddle point has to be formed by the pinching of two spatial branches that respectively originate in the limit of $\omega_i \rightarrow \infty$ from the upper and lower halves of the complex α -plane. If both criteria are met, the instability under consideration is absolute.

In the present work, saddle points were identified using the method proposed by Lesshafft & Marquet (2010). This method requires the solution of the temporal linear stability problem and its adjoint. In order to solve this problem, (2.11) is recast into a temporal eigenvalue problem of the form

$$\mathbf{A}_\omega \hat{\boldsymbol{\phi}} = \omega \mathbf{B}_\omega \hat{\boldsymbol{\phi}}, \quad (2.16)$$

where $\hat{\boldsymbol{\phi}}$ is the eigenfunction vector. The corresponding discrete adjoint problem can then be written as

$$\mathbf{A}_\omega^* \hat{\boldsymbol{\phi}}^+ = \bar{\omega} \mathbf{B}_\omega^* \hat{\boldsymbol{\phi}}^+, \quad (2.17)$$

in which the asterisk and the overbar denote the conjugate transpose and complex conjugate, and the adjoint eigenfunction vector $\hat{\boldsymbol{\phi}}^+$ is normalized so that $\hat{\boldsymbol{\phi}}^{+*} \mathbf{B}_\omega \hat{\boldsymbol{\phi}} = 1$. After both direct and adjoint temporal eigenvalue problems have been solved using the Arnoldi method, the group velocity can be evaluated as

$$\frac{\partial \omega}{\partial \alpha} = \hat{\boldsymbol{\phi}}^{+*} \frac{\partial \mathbf{A}_\omega}{\partial \alpha} \hat{\boldsymbol{\phi}}. \quad (2.18)$$

In the following, a secant method is used to find the roots of zero group velocity. Subsequently, the branch structure around the saddle points is obtained to verify if Briggs' second criterion is met.

3. Experimental configuration and computational set-up

In this paper, we consider a jet flame configuration that was experimentally investigated by Füri *et al.* (2002). The burner consists of a jet nozzle, supplying methane fuel at an axial velocity of $U_0 = 3.8 \text{ m s}^{-1}$. The nozzle exit diameter is $D_0 = 7.5 \text{ mm}$, and the thickness of the nozzle rim is $0.16D_0$. The jet nozzle is surrounded by a coflow, providing a uniform air stream at ambient conditions (with reference temperature of $T_0 = 300 \text{ K}$) through a porous sintered metal plate. The pressure is $p_0 = 1 \text{ bar}$. The operating condition considered in this paper corresponds to the experimental set-up 'Mix 1' of Füri *et al.* (2002). Using the conditions in the fuel stream as reference quantities, the Reynolds number and Froude number are evaluated as $Re = 1770$ and $Fr = 14$, respectively.

Detailed simulations are performed to evaluate the mean flow field for the linear stability analysis. For this, the conservation equations (2.1) are solved in a cylindrical coordinate system, and information about thermochemical quantities is obtained from the FPV model. Spatial derivatives are discretized by a central difference scheme. A fractional-step method is employed to advance the continuity and momentum equations, and the scalar transport equations for mixture fraction and reaction progress variable are solved semi-implicitly. More details on the numerical scheme can be found in Pierce & Moin (2004).

The three-dimensional computational domain is $12D_0 \times 7D_0 \times 2\pi$ in the axial, radial and azimuthal directions, respectively. The computational grid consists of $320 \times 350 \times 32$ grid points in the three respective directions. Velocity inlet conditions for the fuel stream are prescribed by an analytic profile of the form (Michalke 1984)

$$u = \frac{1}{2} \left\{ 1 + \tanh \left(\frac{1 - 2r}{\delta} \right) \right\}, \quad (3.1)$$

with $\delta = 0.1$, and a plug-flow profile is used for the coflow stream with axial velocity of $u = 0.05$. Convective outflow conditions are used at the exit of the domain and free-slip boundary conditions are employed at radial boundaries.

The following analysis is concerned with the axisymmetric ($m = 0$) mode, which was found to be the most unstable mode for this jet flame configuration.

4. Results

Detailed simulations and stability analyses are performed to systematically investigate the effects of mean flow, viscous-diffusive transport properties and reaction chemistry on the disturbance dynamics of a jet diffusion flame. We begin this analysis by first assessing modelling assumptions about the description of the mean flow and transport properties on the jet stability. Comparisons of these results with measurements by Füri *et al.* (2002) will be used to confirm the mathematical model (§ 4.1). In the second part of this study (§ 4.2), we investigate the effects of the chemistry representation and buoyancy on the modal behaviour and the stability characteristics. This investigation considers the same geometric configuration, but employs an adiabatic simulation for the mean flow description.

4.1. Mean flow approximation and viscous-diffusive transport model representation

4.1.1. Model approximations and mean flow evaluation

To systematically elucidate the impact of the mean flow and the transport model on the jet stability, three different model configurations are considered. In these three cases, which are summarized in table 1, assumptions about the mean flow and transport properties are successively relaxed to introduce increasingly more physics into the stability analysis. The first two cases, denoted ‘N1’ and ‘N2’, employ the mean flow description of Füri *et al.* (2002). For this, the mean velocity is prescribed by the hypertangent profile of Michalke (1984) with parameters reported by Füri *et al.* (2002). The mixture fraction follows the same analytic expression, but is shifted radially by $\Delta r = 0.195$ so that the location of the stoichiometric mixture is aligned with the peak temperature location. The temperature profile is directly extracted from the vector graphics plot of the published data (see figure 1 in Füri *et al.* 2002). Temperature and mixture fraction profiles are then mapped onto the progress variable by inverting the FPV flamelet library.

Case	Mean flow	Viscous-diffusive model
N1	Analytic	Chapman approximation
N2	Analytic	Mixture-averaged transport
N3	Simulation	Mixture-averaged transport

TABLE 1. Model approximation to investigate the effects of mean-flow representation and viscous-diffusive transport properties.

Viscous-diffusive transport properties in configuration N1 are described using the Chapman approximation, which relates the dynamic viscosity and diffusivity linearly to temperature:

$$\mu = \mu_0 \frac{T}{T_0}, \quad \nu = \nu_0 \frac{T}{T_0}. \quad (4.1)$$

This assumption is relaxed in the case N2, in which the dependence of the transport properties on temperature and species composition are described using mixture-averaged formulations. Specifically, Wilke's formulation (Wilke 1950; Bird, Stewart & Lightfoot 2007) is used to evaluate the mixture viscosity, and the species mixture diffusivities are evaluated from the approximation due to Hirschfelder & Curtiss (1949),

$$\mu = \sum_{i=1}^{N_S} \frac{X_i \mu_i}{\sum_{j=1}^{N_S} X_j \Phi_{ij}}, \quad \nu_i = \frac{1 - Y_i}{\sum_{j \neq i} X_j / \Upsilon_{ij}}, \quad (4.2)$$

where the tensor Φ_{ij} is a function of the molecular weights and viscosities of all the species involved in the mixture, Υ_{ij} is the binary diffusion coefficient, and X is the species mole-fraction vector.

The third case, 'N3', uses the same mixture-averaged transport model but the perturbations are now expanded around the mean flow, which is obtained from a detailed simulation. The simulation is performed using a non-adiabatic FPV model (Lee *et al.* 2011), in which heat losses to the burner rim are accounted for by introducing a convective heat-loss term and solving the unsteady flamelet equations. The reaction chemistry is described by the detailed GRI-2.11 methane–air kinetics model (Bowman *et al.* 1997), consisting of 279 reactions among 49 species.

A comparison of computed mean flow results and experimental data at the axial location $x = 0.13$ is presented in figure 1. This location corresponds to the position at which the stability analysis is performed. Figure 1(a) shows a comparison of the axial mean velocity; the simulation results are in good agreement with experiments. The dashed line in this figure is the analytic profile that was obtained by Füri *et al.* as a fit to the experimental data, and will be used as the mean flow profile for the cases N1 and N2 in the subsequent stability investigations.

A comparison of the mean temperature is presented in figure 1(b), showing that the simulation results are in good agreement with experiments. In this context it is noted that the peak flame temperature is approximately 800 K below the adiabatic temperature of an unstrained stoichiometric methane–air flame. The reasons for this are non-adiabatic processes near the burner surface. The flame is not fully anchored at the fuel-nozzle exit and stabilizes at the location where heat release and heat losses are in local balance.

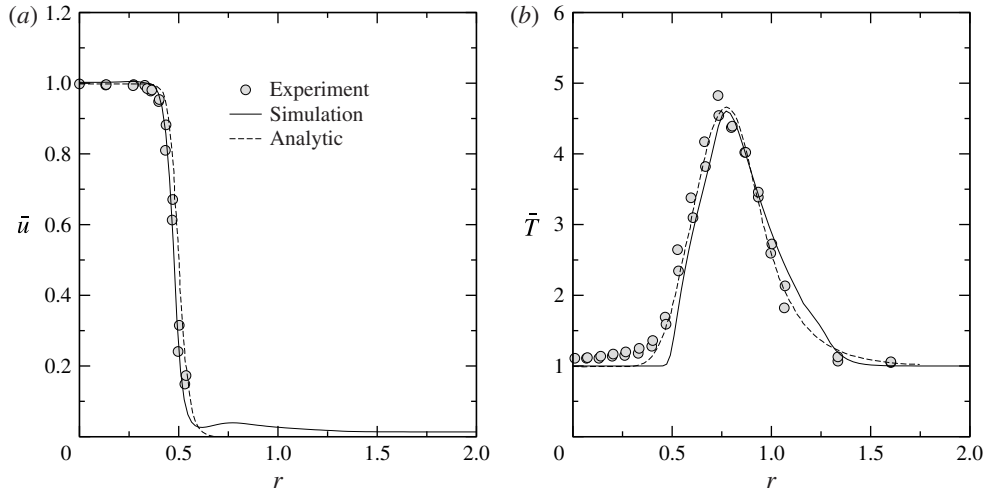


FIGURE 1. Comparison of the radial mean flow results for (a) mean axial velocity and (b) mean temperature at $x = 0.13$. Measurements and analytic profiles are from Füri *et al.* (2002).

The dynamic viscosity is evaluated using the predicted and analytic temperature profiles, and a comparison of the radial profiles for $\bar{\mu}$ is illustrated in figure 2. It can be seen that the viscosity obtained with Chapman's approximation is approximately two times larger at the stoichiometric location compared to the mixture-averaged transport model. It will be shown in the following section that these differences in the transport properties directly affect the inviscid instability mode that develops on the fuel-rich side of the flame.

4.1.2. Linear stability results

This section focuses on the comparison of the stability dynamics for the so-called inner mode, corresponding to a Kelvin–Helmholtz-type instability. A detailed discussion of the buoyancy-driven outer mode is presented in the context of a convective/absolute instability analysis in § 4.2.

A comparison of the results for growth rate and phase speed for the cases N1–N3 is presented in figure 3. Included in this figure are the results from the stability analysis by Füri *et al.* (2002), which was performed using an analytic velocity profile and a one-step chemistry model, in which values for activation temperature, heat release parameter and Damköhler number were adjusted to obtain agreement with measurements.

Overall, for frequencies below $\omega_r = 5$, the results for predicted growth rates are in good agreement with the measurements. However, for frequencies above this value, differences between the three cases become apparent. The lack of agreement at these higher frequencies was also observed by Füri *et al.* (2002), and could be attributed to omitted non-parallel mean flow and nonlinear effects that become relevant with increasing perturbation frequency.

Analysing the effects of viscous-diffusive transport properties shows that the predicted growth rate in the case N1 is smaller than that predicted in the case N2 for frequencies above $\omega_r = 5$. This difference can be attributed to the fact that the viscous-diffusive transport properties predicted using Chapman's approximation are

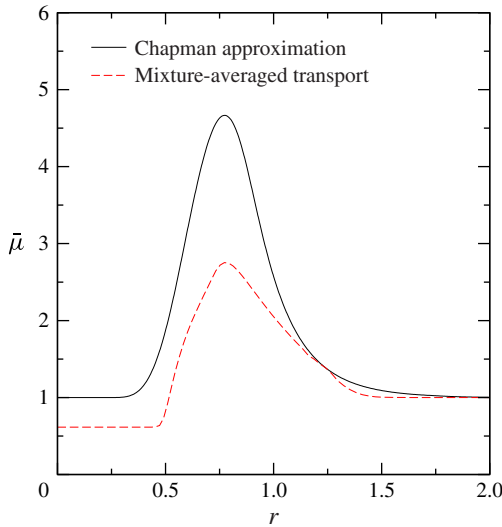


FIGURE 2. (Colour online) Comparisons of dynamic viscosity, evaluated from Chapman's approximation and mixture-averaged transport model at $x = 0.13$.

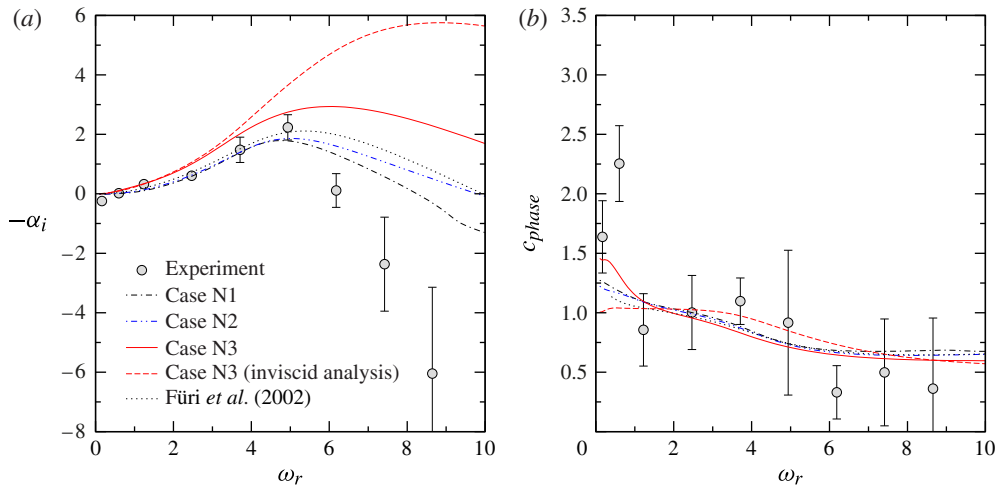


FIGURE 3. (Colour online) Comparison of the results from linear stability analysis with experiments for (a) growth rate and (b) phase speed at axial location $x = 0.13$.

significantly higher than the mixture-averaged transport properties (see figure 2). Since previous findings suggest that this instability mode is related to an inviscid Kelvin–Helmholtz mechanism, this mode is damped by viscosity. In fact, an inviscid analysis (shown by the dashed line in figure 3) predicts a growth rate that is approximately twice as large as the corresponding viscous solution for case N3.

The effect of the mean flow on the growth rate can be assessed by comparing cases N2 and N3 in figure 3(a). The growth rate for the case N3 is consistently higher for all frequencies. A detailed analysis of the mean temperature field showed that this higher growth rate is attributed to the minor shift in the temperature (see figure 1b).

Since the location of the peak temperature is shifted away from the shear layer, the damping effect due to the heat release becomes less effective. In addition, the location of the highest viscosity is also shifted away from the shear layer, further reducing the viscous damping effect.

A comparison of the phase speed as a function of frequency is presented in figure 3(b). The phase speed is computed as

$$c_{phase} = \frac{\omega_r}{\alpha_r}. \quad (4.3)$$

These results show that the instability mode is of convective nature and that the phase speed is relatively insensitive to the underlying modelling assumptions, as all three cases exhibit similar profiles.

4.2. Chemistry representation and buoyancy effects

4.2.1. Model approximations

In the following sections, we investigate the effects of reaction chemistry, thermo-transport property models and buoyancy on the disturbance dynamics. This investigation is conducted in the context of an adiabatic jet flame configuration, which allows us to omit contributions of heat losses that are otherwise difficult to represent consistently in the presence of different reaction mechanisms.

Five different configurations are considered. In the first two cases, denoted by ‘C1’ and ‘C2’, respectively, the methane–air combustion chemistry is described by a one-step global reaction mechanism of the form



and the global reaction rate is represented as (Westbrook & Dryer 1981)

$$k_g = A[\text{CH}_4]^p[\text{O}_2]^q \exp\left\{-\frac{T_a}{T}\right\}, \quad (4.4)$$

where [X] denotes the concentration of species X, A is the frequency factor and T_a is the activation temperature. Numerical values for the rate constants are (Westbrook & Dryer 1981)

$$A = 1.3 \times 10^8 \text{ s}^{-1}, \quad T_a = 24\,358 \text{ K}, \quad p = -0.3, \quad q = 1.3. \quad (4.5)$$

Consistent with the simplicity of the chemical kinetics, in case ‘C1’ the gas is represented as calorically perfect and the transport properties are evaluated using Chapman’s approximation. To investigate the effects of thermal properties on the mean flow and perturbation dynamics, an ideal gas approximation is introduced in case ‘C2’, accounting for temperature-dependent specific heat capacities of the mixture via NASA polynomial expressions (McBride, Zehe & Gordon 2002).

Chapman’s approximation is also employed in case ‘C3’, but the detailed GRI-2.11 mechanism is now considered for modelling the reaction chemistry. Therefore, a comparison between cases C2 and C3 will elucidate the effect of the chemistry model. The fourth case, ‘C4’, contains the highest level of physical fidelity by representing the reaction chemistry using the detailed chemical mechanism, and viscous-diffusive properties are computed from a mixture-averaged formulation. This case is analogous to case N3 that was considered in § 4.1.1.

Case	Chemistry	Transport model	Thermal properties	Fr
C1	One-step chemistry	Chapman approximation	Calorically perfect	∞
C1b	One-step chemistry	Chapman approximation	Calorically perfect	14
C2	One-step chemistry	Chapman approximation	Ideal gas	∞
C3	Detailed chemistry	Chapman approximation	Ideal gas	∞
C4	Detailed chemistry	Mixture-averaged transport	Ideal gas	∞
C4b	Detailed chemistry	Mixture-averaged transport	Ideal gas	14

TABLE 2. Summary of model approximations to investigate the effects of reaction chemistry and thermo-viscous transport on the disturbance dynamics.

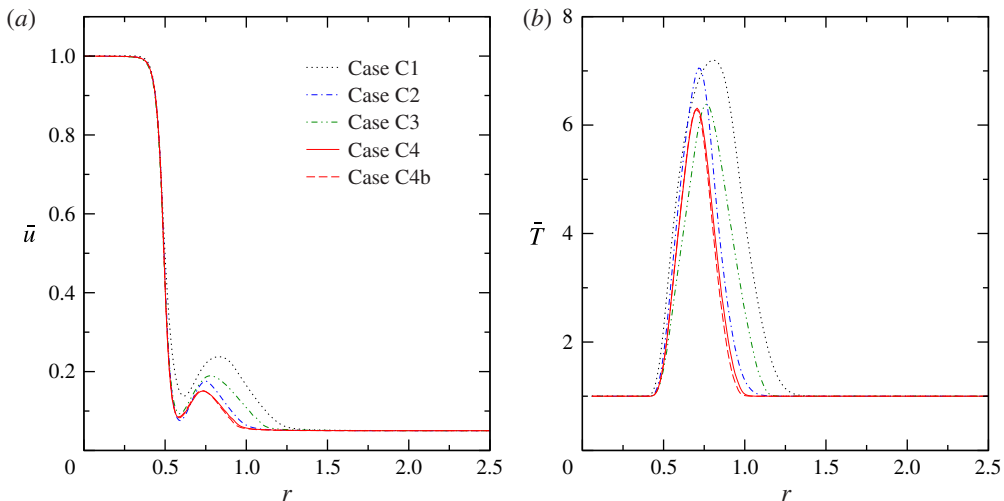


FIGURE 4. (Colour online) Computed radial profiles for (a) mean axial velocity and (b) mean temperature at $x = 0.13$.

Cases C1–C4 are all conducted without consideration of buoyancy effects. To examine the effects of buoyancy on the mean flow and the disturbance dynamics, two additional simulations are conducted. These cases are denoted as ‘C1b’ and ‘C4b’, and use the same chemical mechanism and thermo-viscous transport model as cases C1 and C4. For reference, all investigated configurations together with the modelling assumptions are summarized in table 2.

4.2.2. Mean flow results

Comparisons of computed radial profiles for streamwise velocity and temperature at the axial locations $x = 0.13$ and 1.0 are shown in figures 4 and 5. This comparison illustrates that the mean flow results are affected by the underlying transport properties and thermochemical model descriptions. While this might not be unexpected, it is important to recognize that the influence of these effects is already evident in proximity to the nozzle exit. A comparison of the velocity profiles at $x = 0.13$ (figure 4a) shows qualitative and quantitative differences in the outer region of the shear layer among the cases C1–C4. Most notable is the formation of a localized pocket of high velocity on the oxidizer side. This is a result of the heat-induced

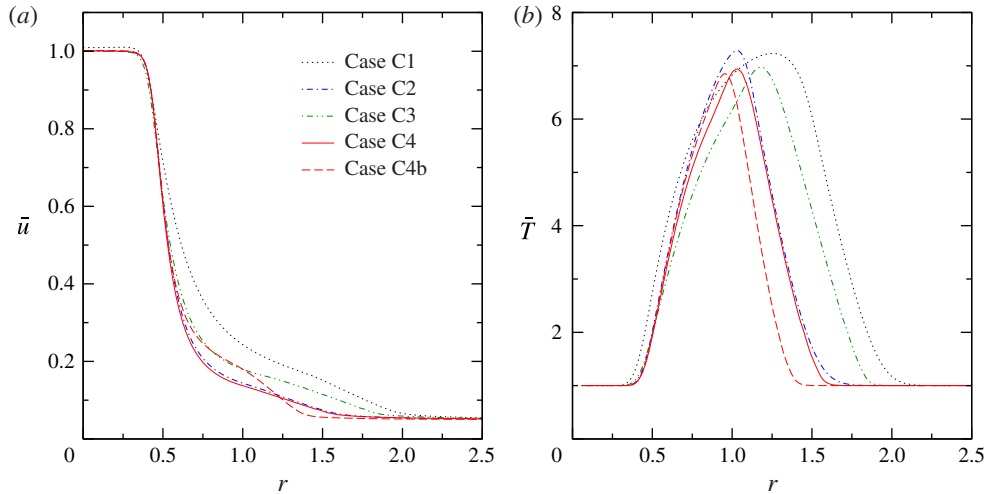


FIGURE 5. (Colour online) Computed radial profiles for (a) mean axial velocity and (b) mean temperature at $x = 1.0$.

volumetric expansion, thereby introducing two additional inflection points. Although to a lesser degree, a similar flow-field behaviour can also be observed in figure 1(a), where it is less pronounced owing to the suppressed heat-induced dilatation as a result of the heat losses to the burner rim.

A comparison of radial temperature profiles, illustrated in figures 4(b) and 5(b), shows considerable differences in the location and structure between the four different flames. Specifically, the maximum flame temperature for the case C1 is higher and the flame is broader than for the other cases. The reasons for this are the calorically perfect gas representation and the global chemistry model, resulting in a significantly different flame structure compared to the ideal gas and detailed chemistry approximations (Williams 1991). This is further illustrated in figure 6, showing a comparison of the temperature profiles in mixture-fraction space at $x = 0.13$ and 1.0. This comparison shows that thermal gas properties primarily affect the fuel-rich side of the flame. In this context, it is noteworthy to point out that the stoichiometric scalar dissipation rate at $x = 0.13$ is approximately an order of magnitude smaller than the quenching value for the detailed chemical model. The reason for the low dissipation rate value is the low-Reynolds-number operating point of this flame and the thick nozzle rim.

The effects of gravity on the mean flow are discussed by comparing temperature fields for cases C4 and C4b. The instantaneous temperature field for the stable jet without consideration of buoyancy (case C4 with $Fr = \infty$) is illustrated in figure 7(a). For this operating condition, the flame remains stable. However, by considering gravitational effects in the computation, the buoyancy initiates an absolute instability in the outer region of the jet, which is illustrated in figure 7(b,c). Figure 7(b) shows an instantaneous result of the axisymmetric temperature field, and figure 7(c) illustrates the corresponding mean temperature field.

The effects of buoyancy on the flow structure in laminar and turbulent jet diffusion flames have been experimentally investigated by Becker & Yamazaki (1978), Han & Mungal (2001) and Muñiz & Mungal (2001), among others. By balancing

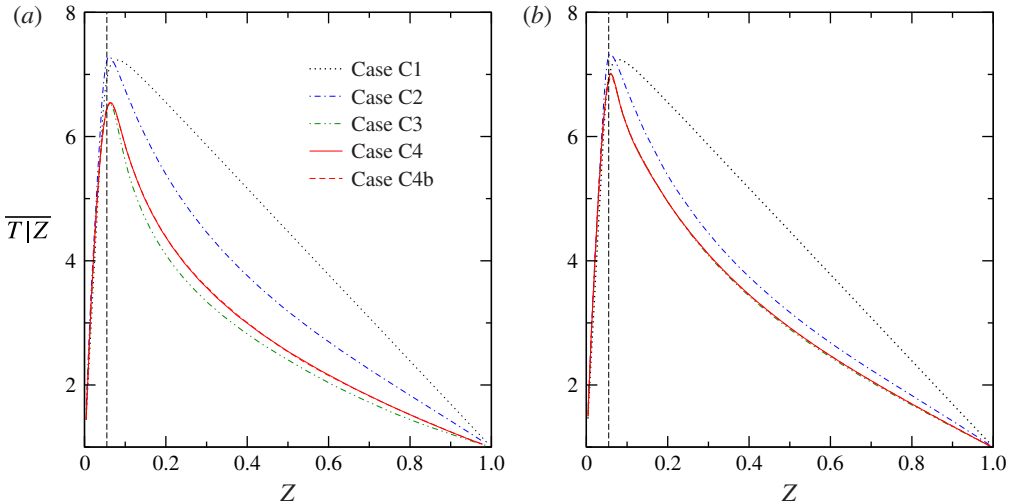


FIGURE 6. (Colour online) Comparison of mixture-fraction conditioned temperature profiles at axial locations (a) $x=0.13$ and (b) $x=1.0$. The vertical dashed line indicates the location of the stoichiometric mixture, $Z_{st}=0.055$.

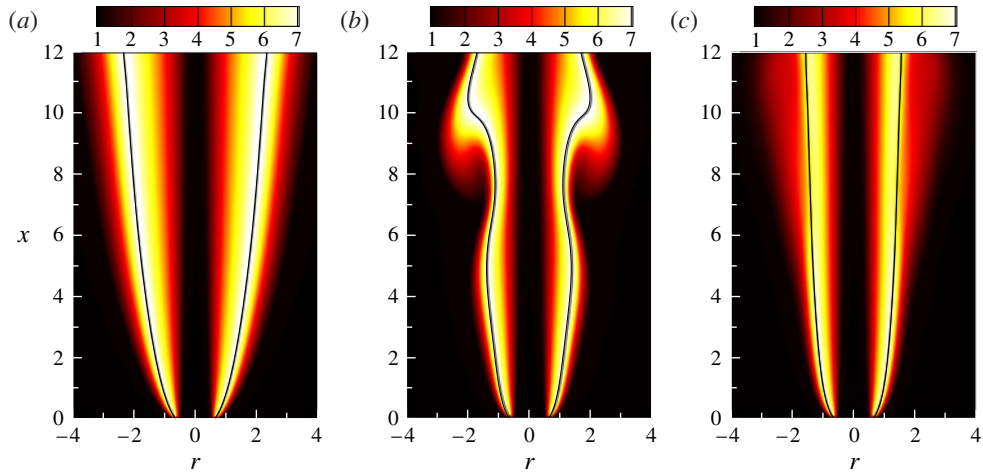


FIGURE 7. (Colour online) Comparison of instantaneous and mean temperature fields: (a) the instantaneous temperature field for case C4; (b) the instantaneous temperature field and (c) the mean temperature field for case C4b with buoyancy effects ($Fr=14$).

buoyancy and inertial forces, Becker & Yamazaki (1978) derived an expression for a self-similarity coordinate that can be written as

$$\zeta = x \left(\frac{\rho_O}{\rho_F} Fr^{-2} \right)^{1/3}, \quad (4.6)$$

where ρ_O/ρ_F is the density ratio between the oxidizer and fuel streams. With this definition, the effects of buoyancy are considered to be irrelevant for $\zeta < 1$. Applying

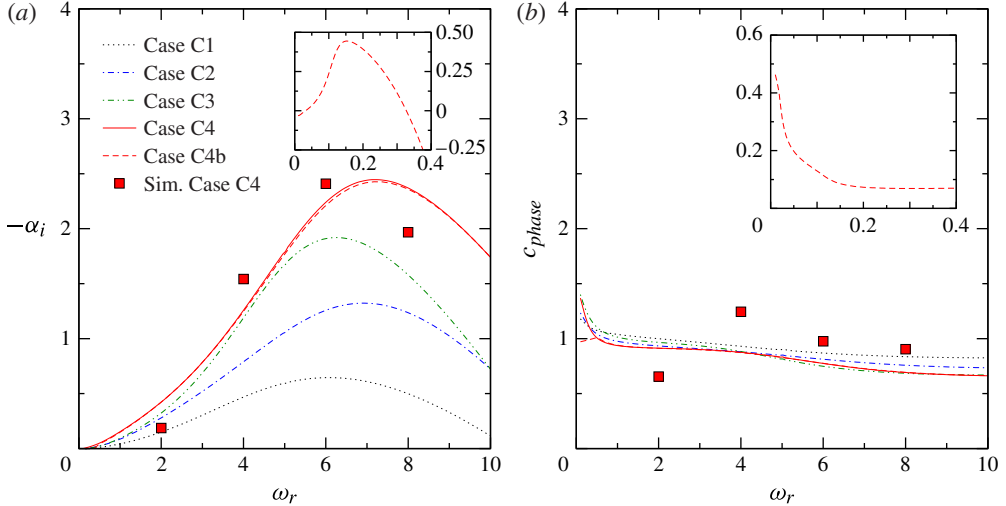


FIGURE 8. (Colour online) Comparison of the results from linear stability analysis for (a) growth rate and (b) phase speed for adiabatic jet flame at axial location $x = 0.13$. Detailed simulation results with harmonically forced inflow condition for case C4 are shown by symbols. The insets show the growth rate and phase speed of the outer buoyancy-driven instability mode for the case C4b.

this criterion to the jet flame configuration C4b suggests that buoyancy effects become relevant for $x > 4.8$. A qualitative comparison of the mean flow profiles between cases C4 and C4b in figure 7 shows that this criterion provides a reasonable estimate. However, it is noted that (4.6) was derived from global force-balance arguments and does not take into consideration buoyancy-induced instabilities, which – dependent on their energy content – directly affect the mean flow structure. Therefore, a refined definition could be derived by relating ζ to the wavelength of the most unstable buoyancy-driven instability mode, namely $\zeta \propto 2\pi/\alpha_r$.

Qualitative comparisons of radial velocity and temperature profiles between cases C4 and C4b show that the effects of buoyancy are largely confined to the outer region of the jet, and the inner momentum-driven shear layer is not affected by gravitational forces. Motivated by this observation, we will separately analyse the inner and outer instability modes. In these investigations, which will be presented in the following sections, we consider the axial location $x = 0.13$, for which mean flow profiles were reported in figure 4.

4.2.3. Inner mode analysis

(a) Growth rate and phase speed

Using the mean flow results obtained from the detailed simulations, linear stability computations for all the cases presented in table 2 are performed. The results of this analysis are illustrated in figure 8, showing the growth rate and phase speed of the most unstable axisymmetric mode as a function of the angular frequency ω_r . It can be seen that the results for all cases agree for $\omega_r < 1$ and deviate increasingly with increasing perturbation frequency. A comparison between the cases C1 and C2 provides direct information about the integrated effect of the thermal properties on the perturbation dynamics. It can be seen that the calorically perfect gas approximation results in a reduced growth rate with increasing perturbation frequency compared to the simulation that employs an ideal gas approximation.

The effect of the reaction chemistry on the growth rate can be assessed by comparing the results for cases C2 and C3. Differences in the mid-frequency range can be observed, which can be attributed to compounding effects of the chemistry-induced shift of the mean flow profiles, a broader flame structure and differences in viscous-diffusive transport properties as a result of the higher peak temperature in the shear-layer region. As such, these results show that the chemical mechanism affects the jet stability through its coupling to the mean flow, which exhibits a strong sensitivity to the thermo-viscous transport properties.

Cases C3 and C4 utilize the same detailed chemical kinetics model, and the differences that are apparent for $\omega_r > 5$ are a result of the different thermo-viscous property models that – although to a lesser degree – were also observed in the context of the instability analysis in § 4.1. In this context it is also noteworthy to mention that the phase speed for the case C4 is lower than that for the cases C1 and C2, which is not observed for the non-adiabatic flame investigations.

Quantitative comparisons of the stability results for the case C4 are provided by presenting detailed simulation results in figure 8. These results are obtained by performing additional computations, in which the axial inlet velocity is harmonically forced with a perturbation of 5 % of the undisturbed inflow at frequencies of $\omega_r = 2, 4, 6$ and 8. Following the procedure outlined in appendix B, the growth rate and phase speed are evaluated using flow-field solutions for radial velocity and velocity magnitude, respectively. A comparison of the results from the stability analysis and detailed simulations for the specific case C4 shows overall good agreement. The detailed computations predict a maximum growth rate around $\omega_r = 5$, and the inner mode remains unstable for higher perturbation frequencies. In this context, it is also noteworthy to mention that, despite the underlying assumptions of the linear stability method, the results remain in good agreement with the detailed simulation results even for perturbation frequencies up to $\omega_r = 8$ (corresponding to a physical frequency of 645 Hz).

To confirm that this inner mode is indeed a shear-layer instability and not affected by buoyancy, we also present the stability results for the case C4b in figure 8. In this computation, buoyancy effects are considered in the simulation, and the results for spatial growth rate and phase speed are identical to those for case C4.

(b) Pinch-point analysis

To determine whether the inner mode is convectively or absolutely unstable, we apply Briggs' method and solve the eigenvalue problem (2.11) for complex frequencies to map local saddle points into the complex α -plane. The result of this investigation is illustrated in figure 9(a), showing solution trajectories for different values of ω_i in the complex α -plane. In this figure, three different saddle points were identified and the corresponding (α_0, ω_0) coordinates are reported in table 3. All three saddle points are located in the lower ω half-plane (i.e. $\omega_{i,0} < 0$). Following Briggs' criterion, the inner mode is therefore convectively unstable and does not represent an absolute instability.

We confirm that these pinch points correspond to the inner mode by performing a perturbation analysis with respect to Fr around the three saddle points. The temporal growth rates $\omega_{i,0}$ of the pinch points as a function of Fr are illustrated in figure 9(b), confirming that the saddle points are indeed insensitive to buoyancy.

Figure 9(a) shows the presence of turning points in the α -plane, which manifest as branch points in the ω -space. Such behaviour was also observed in the work by Papas *et al.* (2003), and can be attributed to an algebraic branch-point structure as

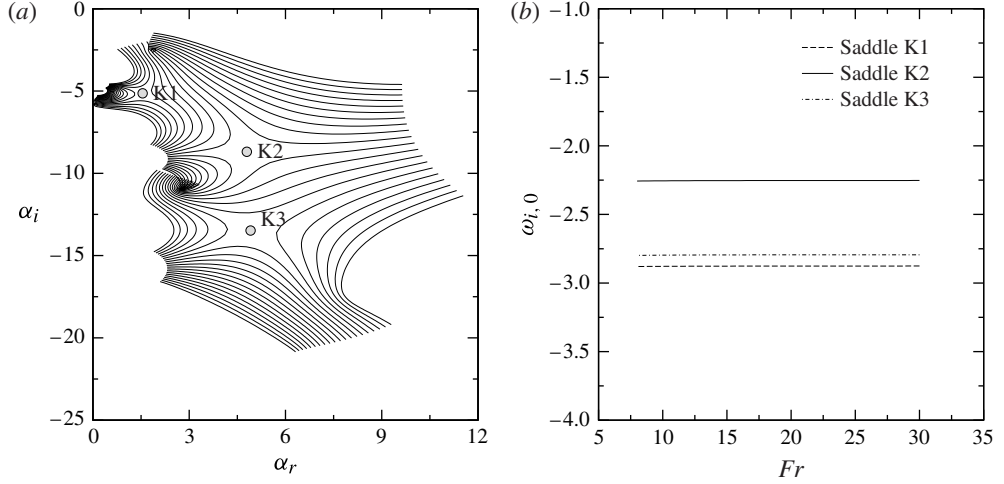


FIGURE 9. Characteristics of the inner mode for case C4b at axial location $x = 0.13$, showing (a) branch structure and (b) the effect of Froude-number variation on instability dynamics.

Saddle point	α_0	ω_0
K1	$1.550 - 5.139i$	$4.607 - 2.877i$
K2	$4.796 - 8.689i$	$5.931 - 2.253i$
K3	$4.914 - 13.475i$	$5.539 - 2.795i$

TABLE 3. Saddle points for inner mode at $x = 0.13$ for the case C4b.

a result of a quadratic ω dependence in the dispersion relation. To demonstrate this, a perturbation equation for \hat{v} , that is similar to a Rayleigh equation, is obtained from (2.11). After neglecting contributions from \hat{Z} and \hat{w} , and omitting viscous and gravitational effects, this equation can be written as

$$(\omega - \alpha \bar{u})^2 V_1 \hat{v} - (\omega - \alpha \bar{u}) V_2 \hat{v} - V_3 \hat{v} = (\omega - \alpha \bar{u}) P_1 \hat{p} + P_2 \hat{p}, \quad (4.7)$$

where the operators V_1-V_3 , P_1 and P_2 are only dependent on the mean flow properties and chemical state:

$$V_1 = \mathcal{F}_\rho \left(\frac{1}{r} + \frac{d}{dr} \right), \quad (4.8a)$$

$$V_2 = i \frac{1}{\mathcal{F}_\rho} \left[\frac{d\bar{C}}{dr} \frac{\partial \mathcal{F}_{\dot{\omega}C}}{\partial C} + \frac{d\bar{Z}}{dr} \frac{\partial \mathcal{F}_{\dot{\omega}C}}{\partial Z} \right] \frac{\partial \mathcal{F}_\rho}{\partial C} - \alpha \mathcal{F}_\rho \frac{d\bar{u}}{dr} + \frac{\partial \mathcal{F}_{\dot{\omega}C}}{\partial C} \left(\frac{1}{r} + \frac{d}{dr} \right), \quad (4.8b)$$

$$V_3 = i\alpha \frac{\partial \mathcal{F}_{\dot{\omega}C}}{\partial C} \frac{d\bar{u}}{dr}, \quad (4.8c)$$

$$P_1 = -i\alpha^2, \quad (4.8d)$$

$$P_2 = -\frac{\alpha^2}{\mathcal{F}_\rho} \frac{\partial \mathcal{F}_{\dot{\omega}C}}{\partial C}. \quad (4.8e)$$

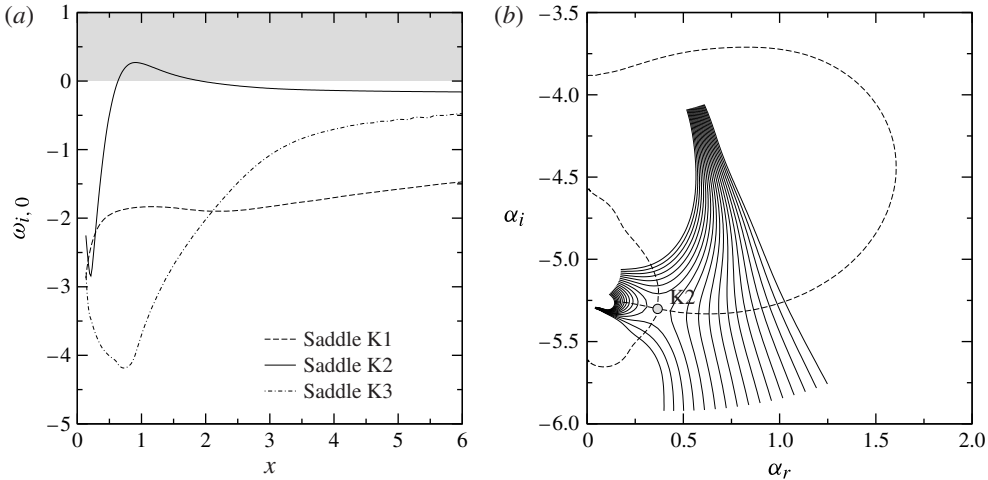


FIGURE 10. Pinch-point analysis for inner mode. (a) Temporal growth rate of saddle points along axial distance x , with shaded area indicating the region of absolute instability. (b) Branch structure around saddle point K2 at $x = 1.0$; solid lines denote curves of constant ω_i and dashed lines are limiting pathways parallel to imaginary ω -axis.

The simplified equation shows that the terms involving $\partial_C \mathcal{F}_{\omega_C}$ are responsible for the algebraic branch-point structure, and equations (4.8) become linear for non-reacting flow conditions, that is, $\partial_C \mathcal{F}_{\omega_C} = 0$. This simplified argument indicates that the chemical source term is a potential source of this branch cut. However, it is noted that this argument was derived by omitting higher-order contributions due to viscosity, gravity and other secondary effects. A more detailed analysis, which is beyond the scope of this work, is required to fully characterize the origin and dynamics of these branch cuts.

Having found that the inner mode at $x = 0.13$ is convectively unstable, we are now interested in determining its stability characteristics with increasing distance away from the nozzle. For this, the trajectory of the pinch points in the complex α -plane is tracked as a function of axial position x . The temporal growth rate of the pinch points along this trajectory is shown in figure 10(a), and it can be seen that the saddle points K1 and K3 remain convectively unstable ($\omega_{i,0} < 0$). Interestingly, over a small axial range $0.6 \leq x \leq 2$, the saddle point K2 crosses from the lower to the upper ω half-plane, suggesting that this inner mode becomes absolutely unstable. A further analysis of the branch structure revealed that this saddle point violates the necessary Briggs' condition. This is illustrated in figure 10(b) for the specific axial location $x = 1.0$; solid lines denote pathways for constant ω_i and dashed lines are the limiting pathways parallel to the imaginary ω -axis. It can be seen that the two spatial branches that form the saddle point originate from the lower α half-plane, confirming that the inner mode remains convectively unstable.

(c) Mode reconstruction

The stability analysis is further extended to obtain an approximate spatial representation of the inner mode structure. In this analysis, the non-buoyant case C4 is considered. Following the formulation presented by Oberleithner *et al.* (2011), we approximate the spatial mode structure from the solution of local linear stability

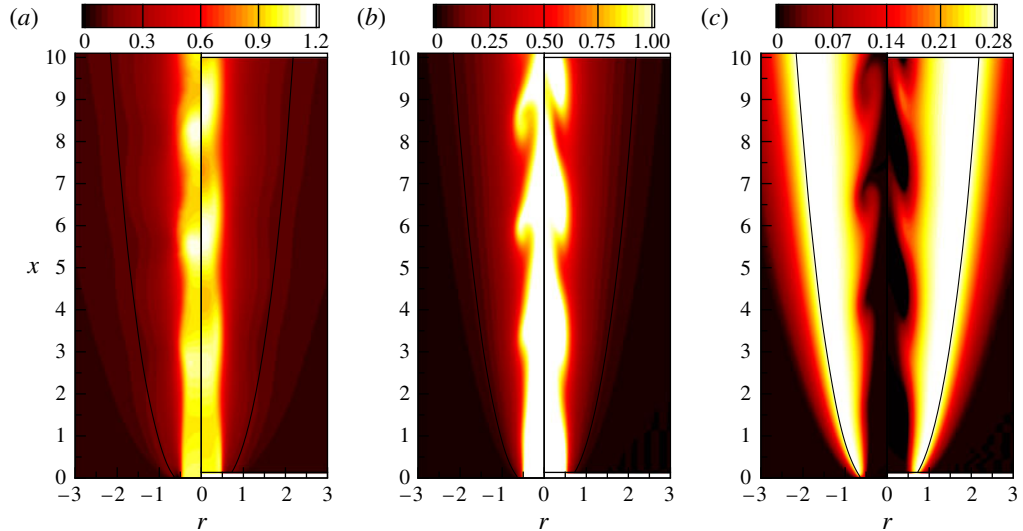


FIGURE 11. (Colour online) Comparison of instability modes from detailed simulation (left half of each panel) and reconstruction from linear stability analysis (right half of each panel, as mirror image) for (a) axial velocity, (b) mixture fraction and (c) progress variable, for case C4 with forcing frequency $\omega_r = 2$.

results along x :

$$\phi'(t, x) = \text{Re} \left(\frac{\hat{\phi}(r; x)}{|\hat{\phi}(r; x)|} \exp \left\{ i \left(\int^x \alpha(\zeta) d\zeta + m\theta - \omega t - \arg(\hat{\phi}(r; x)) \right) \right\} \right), \quad (4.9)$$

where $\text{Re}(\cdot)$ denotes the real part of the argument, $|\hat{\phi}| = \hat{\phi}\bar{\hat{\phi}}$ is the modulus of $\hat{\phi}$, and the last term in the exponent is introduced to phase-align the perturbation eigenfunctions. It is noted that this expression does not take into consideration the spatial growth of the eigenfunction, which would require a multi-scale expansion (Crighton & Gaster 1976) and is beyond the scope of this work. The results from this analysis are compared against detailed simulations. These detailed simulations are performed by harmonically forcing the axial velocity at the inlet with a perturbation of 5 % of the undisturbed inflow.

Comparisons of these results against detailed simulation data are presented in figures 11 and 12. Two perturbation frequencies, namely $\omega_r = 2$ and 5, are considered in this investigation. In these figures, the results for axial velocity, mixture fraction and progress variable are shown; simulation results are presented on the left, and the reconstructed inner mode from the stability analysis is shown as a mirror image on the right.

This direct comparison shows that the results from the stability analysis are overall in reasonable agreement with the detailed simulations. Apart from the modal drift with increasing downstream distance, the instability wavelength is well captured by the mode reconstruction. The reason for this acceptable agreement is that this inner mode is advected by the shear-layer mean flow ($\bar{u} \sim c_{\text{phase}} = \omega_r/\alpha_r$; see figure 8b), which remains relatively insensitive to the radial location.

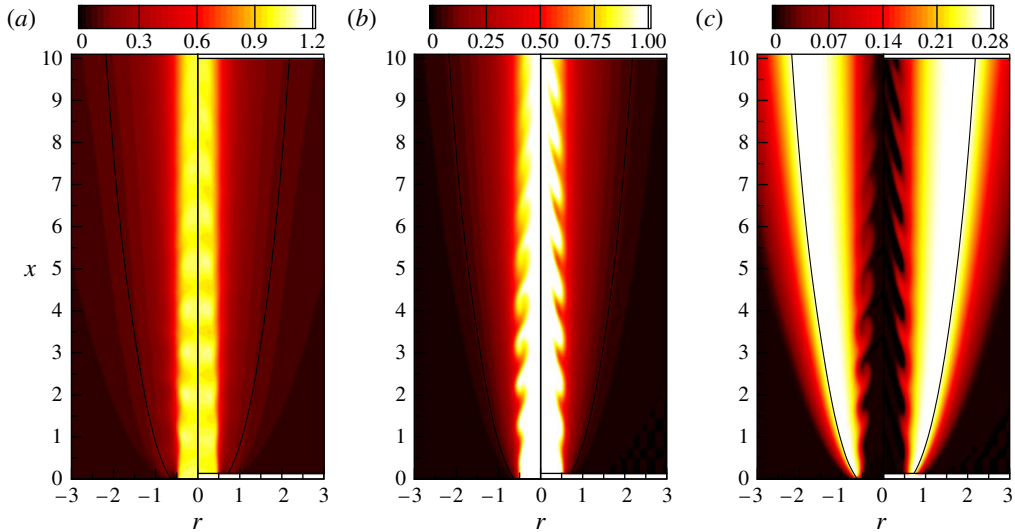


FIGURE 12. (Colour online) Comparison of instability modes from detailed simulation (left half of each panel) and approximated reconstruction from linear stability analysis (right half of each panel, as mirror image) for (a) axial velocity, (b) mixture fraction and (c) progress variable, for case C4 with forcing frequency $\omega_r = 5$.

With increasing frequency, nonlinear effects become increasingly important. This is illustrated in figure 12, showing the instantaneous flow-field structure for the perturbation frequency $\omega_r = 5$. Similar to the results presented in figure 11, it can be observed that the general mode shape is well captured; however, discrepancies in the predicted growth of the instability mode are apparent, which increase with increasing downstream distance. These differences may be attributed to non-parallel mean flow effects that are not considered in this analysis. In addition, it is also noted that nonlinear effects in the combustion chemistry are not considered. While this linearization is at the heart of the stability analysis and consistent with the formulation, such effects can potentially play a role in regions that are affected by heat release and transient combustion processes.

4.2.4. Outer mode analysis

From the detailed simulations of the buoyant jet flame case C4b, it was observed that a self-excited outer mode develops in the presence of buoyancy (see figure 7b). This self-sustained oscillation suggests the presence of an absolute instability. To investigate this further, the stability analysis is extended with the objective to investigate (i) whether the outer mode is convectively or absolutely unstable and (ii) whether a transition point exists between these regimes.

Unlike the Kelvin–Helmholtz-type instability, which is located in the shear-layer region, the outer mode is controlled by density differences and is therefore confined to the region of stoichiometry at the outer side of the flame. However, the entrainment of air at the outer side of the jet flame introduces radial velocity components that are incompatible with the parallel mean flow assumption and not considered in the local stability analysis. Recognizing this limitation, we therefore expect that these results are only qualitatively correct, but nevertheless provide meaningful trends regarding the

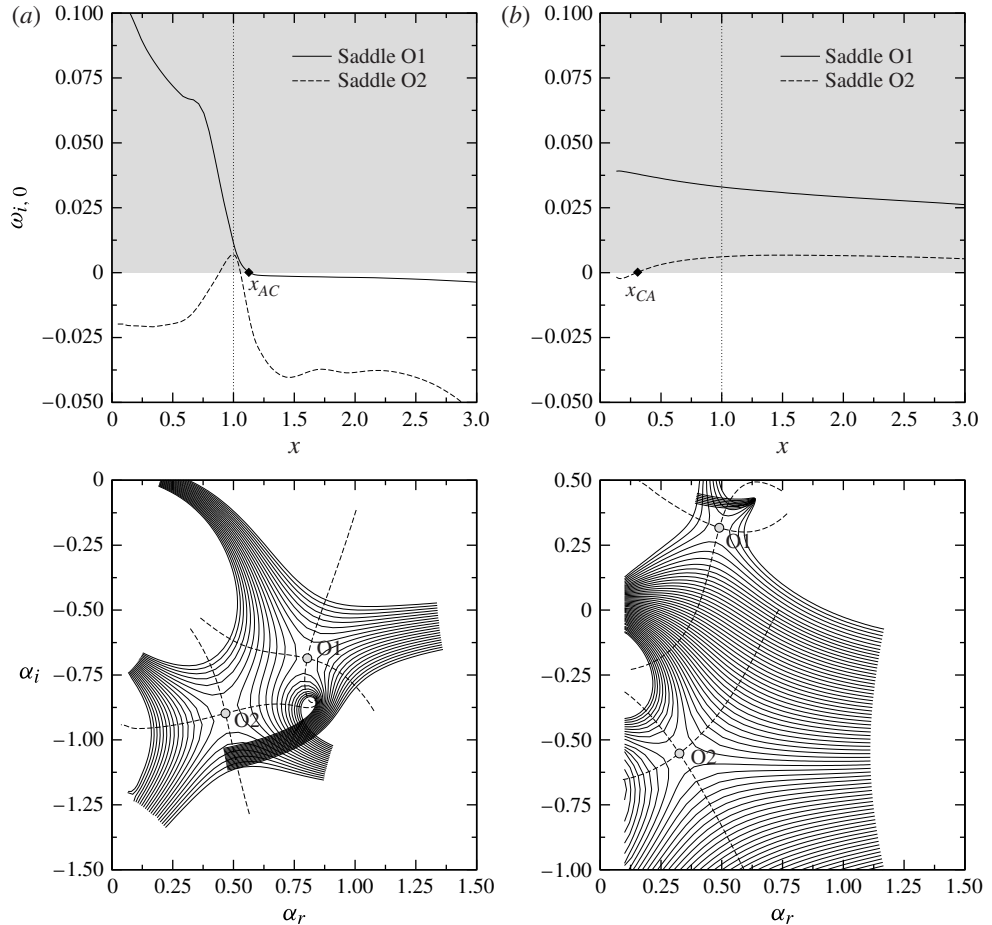


FIGURE 13. Pinch-point analysis for (a) case C4b and (b) case C1b. Upper panels show temporal growth rate of saddle points along axial location x , with shaded area indicating the region of absolute instability. The critical transition points between convective/absolute (x_{CA}) and absolute/convective (x_{AC}) modes are indicated by black symbols. Lower panels show branch structure at $x = 1.0$ (vertical dashed lines in upper panels). Solid lines denote curves of constant ω_i and dashed lines are limiting pathways parallel to imaginary ω -axis.

instability dynamics of the buoyancy-driven mode. Multi-scale analysis (Crighton & Gaster 1976; Crighton *et al.* 1992; Nayfeh 2000) or global stability theory (Huerre & Monkewitz 1990; Chomaz 2005; Theofanis 2011) can be employed to account for these non-parallel effects. This, however, is beyond the scope of this contribution and the subject of future work.

Simulations of the adjoint stability problem are conducted to track the pinch points in the complex α -plane as a function of x . The imaginary part of the frequency for the two most unstable pinch points along the axial distance x is shown in the upper panel of figure 13(a). The region for which the necessary condition that $\omega_i > 0$ is fulfilled is shown in grey. The results suggest that the saddle point O1 is absolutely unstable up to the location $x = 1.15$, at which a transition to the convectively unstable regime occurs. The axial location of the transition from absolute to convective regime

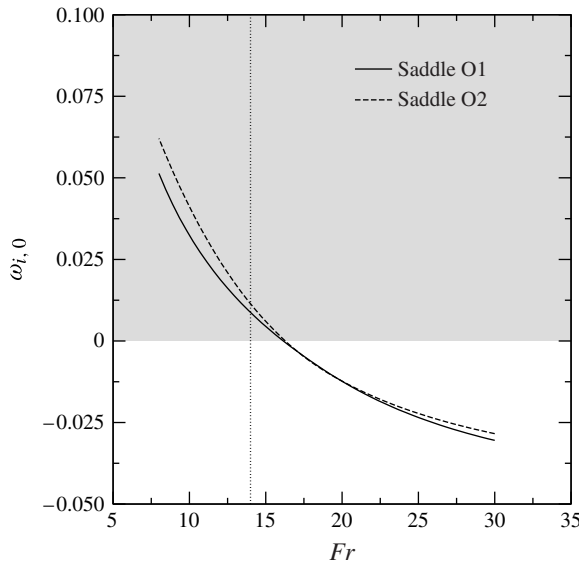


FIGURE 14. The effect of Froude number on the instability dynamics of the outer mode at $x = 1.0$ for case C4b. The shaded area indicates the region of absolute instability.

is denoted by x_{AC} . To confirm that O1 is convectively unstable, we also evaluate the branch structure at $x = 1.0$. These results are presented in the lower panel of figure 13(a), confirming that the spatial branches, which form the pinch point O1, originate from the lower and upper half-planes. This figure also shows that the second saddle point violates Briggs' criterion, so that it can be concluded that the pinch point O2 remains convectively unstable over the entire axial distance. The spatial evolution of $\omega_{i,0}$ indicates that the case C4b is absolutely unstable from the nozzle inlet. Using the criterion established by Chomaz, Huerre & Redekopp (1988), the global frequency, $\omega_{r,G}$, is evaluated as 0.15. An additional condition for the destabilization of the global mode requires that the region of absolute instability needs to exceed the instability wavelength in order for the global mode to be self-excited (Chomaz *et al.* 1988). Although the spatial extent of the absolute instability region does not fulfil this requirement, the detailed simulations indicate the presence of a global mode. The frequency of this mode was evaluated from the simulation as $\omega_{r,G} = 0.19$, and the prediction from the stability results are within 21% of this value. The presence of the self-excited mode may be attributed to the fact that the flow, shown in figure 13(a), is only marginally convectively unstable for $x > x_{AC}$.

To further assess the sensitivity of the nature of the outer mode, a perturbation analysis with respect to the Froude number is conducted. The results of this study for the saddle points O1 and O2 at $x = 1$ are shown in figure 14. Compared to the inner mode (see figure 9b), it can be seen that both pinch points exhibit considerable dependence on changes in Froude number. In particular, with increasing Froude number, $\omega_{i,0}$ transitions from the upper to the lower complex ω -plane, becoming convectively unstable. This is consistent with our physical understanding and confirmed by simulations that buoyancy-driven instabilities reduce as Fr increases.

The sensitivity of the absolute stability behaviour to the representation of transport properties and reaction chemistry is further investigated by performing simulations of the case C1, in which buoyancy effects are considered by setting the Froude number

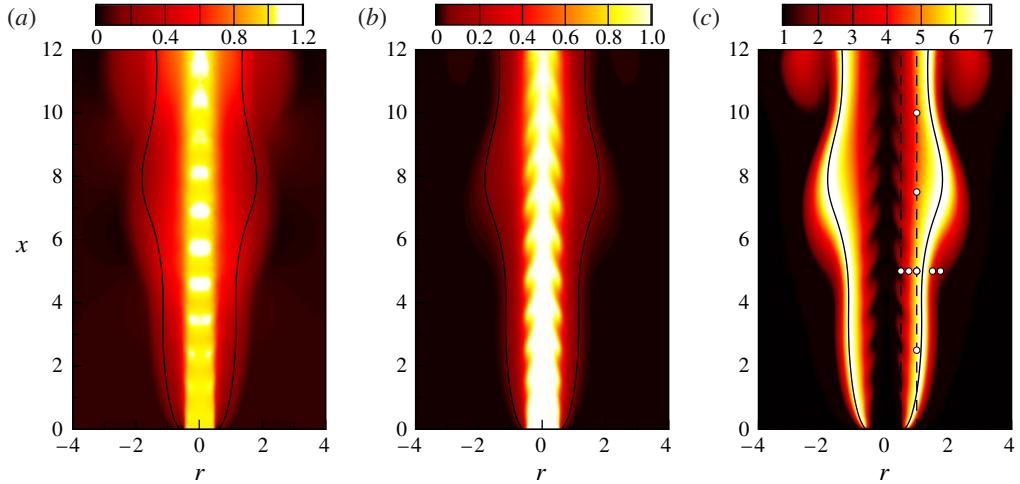


FIGURE 15. (Colour online) Instantaneous flow field for harmonically forced case C4b, showing (a) axial velocity, (b) mixture fraction and (c) temperature. The isocontour of the stoichiometric mixture is shown by the solid lines; the dashed lines and symbols denote measurement locations for spectral analysis.

to $Fr = 14$. Following our convention, this configuration is denoted as case C1b (see table 2). The results for the streamwise evolution of the temporal growth rate and branch structure at $x = 1$ are shown in figure 13(b). The pinch-point analysis indicates that the saddle point O1 does not fulfil Briggs' criterion (requiring that the two branches originate from the two half-planes for $\omega_i > \omega_{i,0}$), and only the saddle point O2 provides information about the absolute/convective behaviour. Compared to the results for the case C4b, it can be seen that this configuration exhibits a small region of convective instability at the nozzle exit, which is followed by an absolute instability region. The location of the transition between convective and absolute instability is denoted by x_{CA} . Applying the frequency criterion of Pier & Huerre (2001) to this case, the global frequency $\omega_{r,G}$ is evaluated at this transition point to be 0.086, which is approximately two times smaller than the global frequency for C4b.

4.2.5. Nonlinear instability dynamics

The focus of this investigation is to examine the modal coupling and nonlinearities that are not described by the linear stability analysis. For this, an additional simulation of the case C4b is performed in which the axial velocity at the fuel inlet is harmonically forced at a constant frequency of $\omega_r = 5$ and amplitude of 2.5% of the mean flow.

Instantaneous flow-field results for axial velocity, mixture fraction and temperature are illustrated in figure 15, showing the spatial evolution of the inviscid inner mode and the buoyancy-driven outer mode, which was shown to be absolutely unstable at the nozzle exit.

Probe measurements of the temperature are extracted from the simulation, and the locations are indicated by symbols in figure 15(c). The results for the temporal evolution of T at these locations are presented in figure 16. Shown in figure 16(a) are measurements across the shear layer, highlighting the change in frequency and signal amplitude between the regions associated with the inner shear layer, stoichiometric

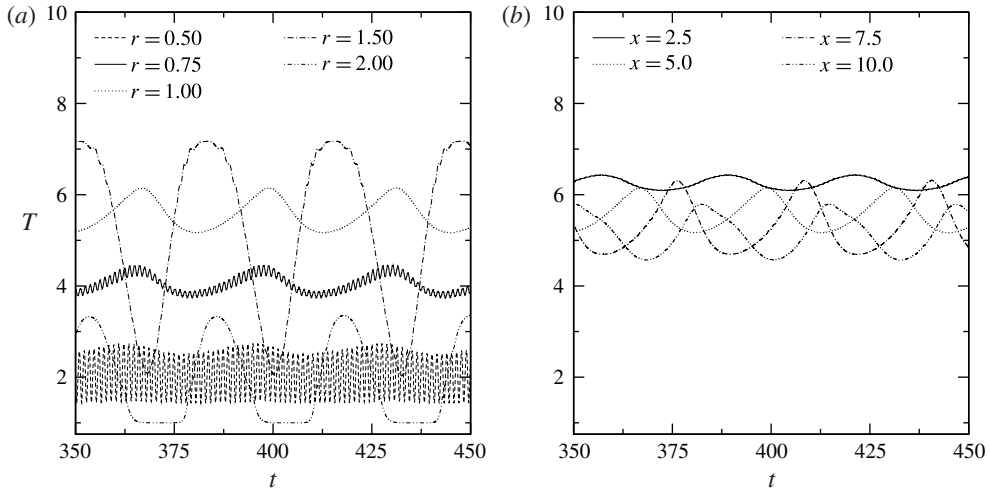


FIGURE 16. Temporal evolution of temperature at different probe locations in the jet flame: (a) radial direction, at $x = 5.0$; (b) axial direction, at $r = 1.0$.

reaction zone and outer shear layer. Figure 16(b) shows temperature signals at four locations along the jet downstream direction. It can be seen that, dependent on the spatial location, the perturbation amplitude of the temperature signal can reach values in excess of 50 % of the mean value. This is a direct consequence of the sensitivity of the temperature and other thermochemical quantities to mixture fraction and progress variable. It is also noteworthy to point out that the thermochemical state variables are bounded, so that the perturbation amplitude of temperature saturates, which is most apparent for $r = 2$ in figure 16(a). Such effects are not easily incorporated into the linear stability analysis, and care must be taken when interpreting the stability results.

Fourier transformations of the temperature signal are performed, and the results from this analysis are presented in figure 17, showing $\log_{10}(|\mathcal{F}(T)|)$ as a function of angular frequency and axial distance. The Fourier spectrum along the jet lip line (figure 17a) shows a pronounced peak at the fundamental forcing frequency $\omega_r = 5$ and the downstream development of higher harmonic modes. However, while the spectrum around the forcing frequency broadens due to spectral energy transfer, the higher harmonics rapidly decay beyond $x = 8$ and 5, respectively. By moving further away from the centreline, the spectral signature of the inviscid mode decays and the outer mode becomes prominent, which is shown in figure 17(b).

The low-frequency peak at $\omega_r = 0.18$ corresponds to the buoyancy mode, and this value is in agreement with the most unstable mode from the linear stability analysis (see insets in figure 8a). The spectral content of this mode increases with increasing downstream distance. This can also be seen in figure 17(b), showing the frequency spectra along the jet sideline at $r = 1$. At this radial location, the contributions of the inner mode become insignificant, and the outer mode is most prominent, which is seen from figure 16(b).

To investigate the coherent structures that are associated with the inner and outer instability modes, a proper orthogonal decomposition (POD) analysis is performed. The POD method, also known as principal component analysis or Karhunen–Loëve expansion, is frequently employed to obtain low-order representations of the complex flow field by decomposing a sequence of data into a set of orthogonal eigenfunctions

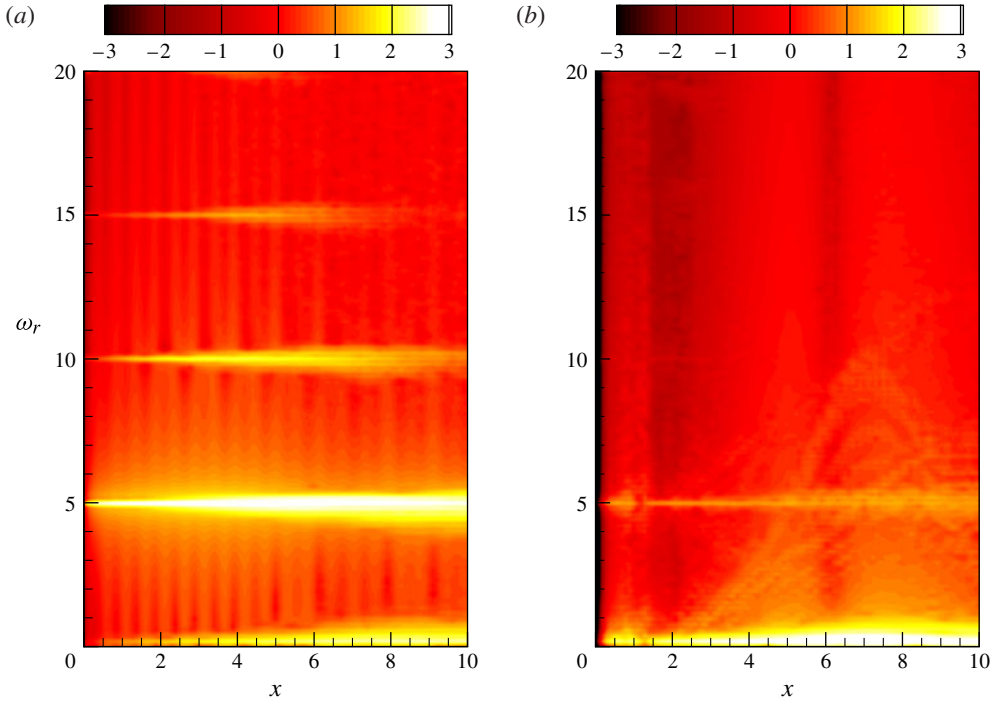


FIGURE 17. (Colour online) Frequency spectrum for temperature along the axial distance through the jet for radial locations (a) $r=0.5$ and (b) $r=1.0$ (corresponding to the dashed lines in figure 15c).

$\{\Theta_i\}$ that minimize the mean square error between the data – in the present case the temperature T – and the POD modes (Holmes, Lumley & Berkooz 1998):

$$\iint \left((T(t, \mathbf{x}) - \bar{T}(\mathbf{x})) - \sum_{i=1}^N a_i(t) \Theta_i(\mathbf{x}) \right)^2 d\mathbf{x} dt \rightarrow \min, \quad (4.10)$$

where $\{a_i\}$ are the time coefficients of the POD modes. In the following, the snapshot POD method due to Sirovich (1987) is employed to evaluate the POD modes from a set of time-discrete flow-field data from the detailed simulation. This dataset consists of 3000 snapshots at a time increment of $\Delta t = 0.025$, spanning approximately two periods of the outer mode. The fine temporal resolution is necessary to capture the inner instability mode. The solution of the POD method can be formulated as an eigenvalue problem, with eigenvalues representing the fluctuating energy content of the POD modes. In this context it is noted that the term ‘energy’ is used loosely since temperature as primitive quantity does not represent a thermodynamically meaningful energy. Nevertheless, it will be shown subsequently that this analysis allows us to extract useful information about the dynamics of the inner and outer instability modes.

The eigenvalue spectrum of the first 18 most energetic POD modes is illustrated in figure 18(a), showing that the first four POD modes alone contain more than 99 % of the energy. Furthermore, it can be seen that the modes come in pairs, indicating that each pair represents an advecting wave. The phase plots of the POD time coefficients are shown in figure 18(b). The phase plot in the upper left panel of figure 18(b)

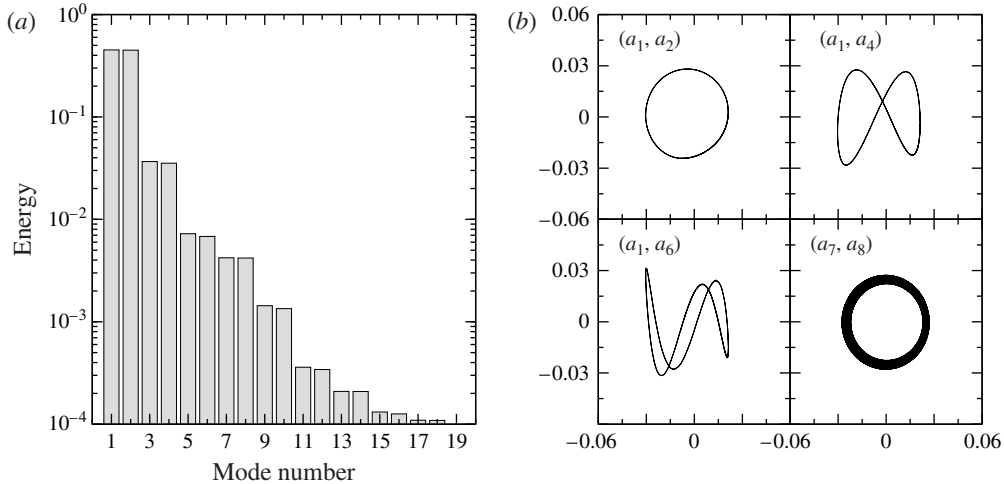


FIGURE 18. POD analysis showing (a) POD spectrum of temperature modes and (b) phase plots of the time coefficients of the POD modes.

shows that the time coefficients a_1 and a_2 evolve on a periodic orbit, representing an oscillatory behaviour. From the phase plots that are generated by the mode pairs (a_1, a_4) and (a_1, a_6) , it can be deduced that the second and third POD modes are higher harmonics, having lower energy content. This indicates that the first three mode pairs are correlated, and the spatial structure of the corresponding POD eigenfunctions (with odd-numbered modes shown in figure 19a–c) shows that these modes represent the outer buoyancy-driven instability mode.

Further analysis of the POD results showed that the inner instability mode is represented by the fourth POD mode pair, corresponding to modes 7 and 8 in figure 18(a). This mode pair contains less than 1 % of the energy. The eigenfunction of one of these POD modes is illustrated in figure 19(d), capturing the features of the inner instability mode that are associated with the initial growth and viscous damping beyond $x = 8$ (cf. figure 15c). The phase plot of the corresponding time coefficients a_7 and a_8 are presented in the lower right panel of figure 18(b), showing that this mode pair evolves on a periodic orbit with a period corresponding to that of the forcing frequency.

This empirical mode analysis shows that only eight POD modes are sufficient to capture the dominant features of this forced buoyancy-driven jet diffusion flame. This information could be used to develop low-order control models (Holmes *et al.* 1998; Bergmann, Bruneau & Iollo 2009), providing opportunities for further investigations.

5. Conclusions

This work addressed the sensitivity of the instability behaviour of jet diffusion flames to the representation of the reaction chemistry, mean flow description and fidelity of the thermo-viscous-diffusive transport models. To this end, a flamelet formulation was integrated into linear stability analysis to systematically examine the effects of the stability behaviour to specifications of the mean flow description, thermo-viscous transport properties, reaction chemistry and buoyancy. The interaction between these processes is schematically illustrated in figure 20.

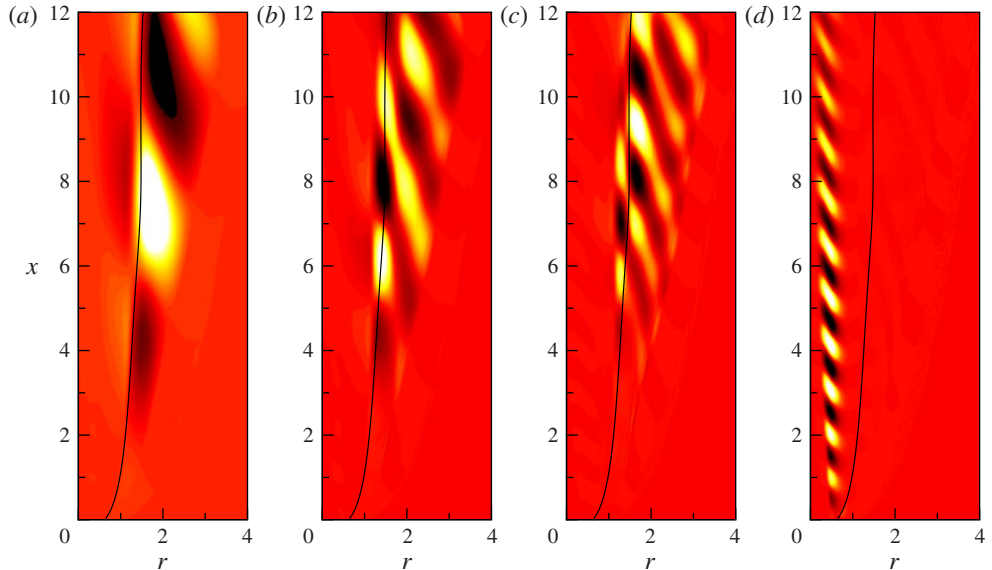


FIGURE 19. (Colour online) First four odd-numbered POD eigenfunctions obtained from the detailed simulation results of the periodically forced case C4b: (a) mode 1; (b) mode 3; (c) mode 5; (d) mode 7.

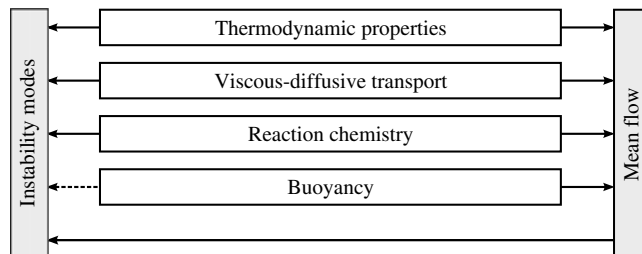


FIGURE 20. Schematic of the coupling mechanisms between physical combustion processes, mean flow, buoyancy and instability dynamics in jet diffusion flames.

Unlike linear stability formulations in which mean flow profiles and model parameters are often adjusted to describe experimental observations, the model presented herein enables a consistent representation of reaction chemistry and transport properties for the mean flow description and perturbation analysis. By introducing additional physical combustion submodels, this formulation can potentially be employed to study more complex instability mechanisms in diffusion flames, such as cellular and thermo-diffusive instabilities, radiation or edge-flame stabilization. By constructing the flamelet solution space from premixed flames, this model can also be extended to the analysis of premixed instabilities, which are known to have a considerably richer instability facet than diffusion-controlled flames.

The model was applied to a coaxial jet diffusion flame configuration that was experimentally investigated by Füri *et al.* (2002). Following a model validation by comparing the simulation results with measurements and the results from stability investigation by Füri *et al.*, investigations of an adiabatic flame configuration

were performed to investigate the effects of the thermo-viscous-diffusive transport, mean flow representation and reaction chemistry on the instability behaviour. Detailed simulations were performed to obtain mean flow properties. In the present investigation, three model configurations were considered. The first study examined the effects of the viscous-diffusive transport on the instability dynamics either by representing the molecular transport properties in terms of Chapman's approximation or by using a mixture-averaged description, accounting for the dependence on temperature and mixture composition. It was found that the growth rate of the Kelvin–Helmholtz-type instability mode in the inner shear-layer region exhibits a sensitivity to the specification of the thermo-viscous-diffusive transport properties. This is mainly attributed to the fact that higher values for viscosity and diffusivity using Chapman's approximation result in a damping of the hydrodynamic instability. This sensitivity is frequency-dependent and reduces with decreasing perturbation frequency. By contrast, the phase speed exhibits only modest sensitivity to specification of the transport properties. The stability results were compared with detailed simulation results. It was shown that the inviscid instability mode remains convectively unstable for frequencies above $\omega_r = 8$.

The effects of the mean flow description on the instability dynamics were examined in the second study, and detailed simulations were performed to obtain mean flow quantities that were used for the stability analysis. For the present configuration, it was found that the inviscid instability mode exhibits a strong sensitivity to the mean flow representation, which was attributed to the presence of additional inflection points that are typically not considered in an analytic mean flow description.

At the highest level of physical complexity that is contained in this formulation, the third study considered the representation of the reaction chemistry on the stability behaviour. Comparisons with a detailed chemical-kinetics model (case C4) showed that for the present configuration the use of a standard one-step chemistry representation (cases C1 and C2) in combination with a simplified viscous-diffusive transport model can significantly attenuate the most unstable inviscid instability mode. This could be attributed to the broader flame structure predicted by the one-step chemistry model, and is further exacerbated by the representation of the transport properties. A pinch-point analysis was performed to determine the nature of the instability modes. From this investigation, it was found that the inner shear-layer-driven instability mode is convectively unstable. The outer buoyancy-driven instability is initially absolutely unstable but transitions to become convectively unstable, and the axial location of the transition point is Froude-number-dependent.

This investigation was complemented by a POD analysis. The outer instability mode was captured by the first three POD mode pairs, corresponding to the fundamental and higher harmonics, and the inviscid instability mode was represented by the fourth POD mode pair, which evolves on a periodic orbit at an angular velocity equal to the forcing frequency.

Acknowledgements

The authors gratefully acknowledge financial support through the National Science Foundation (NSF) CAREER program with Award No. CBET-0844587 and the Office of Naval Research (ONR) under Grant No. N00014-10-1-0717. This work used the Extreme Science and Engineering Discovery Environment (XSEDE), which is supported by NSF Grant No. ASC130004.

Appendix A. Coefficient matrixes for linear stability analysis

The coefficient matrix \mathbf{A} in (2.11) takes the form

$$\mathbf{A} = \begin{bmatrix} 0 & 0 & A_{1,3} & 0 & A_{1,5} & 0 & 0 & A_{1,8} & 0 & A_{1,10} & 0 \\ 0 & 1 & 0 & 0 & 0 & 0 & 0 & 0 & 0 & 0 & 0 \\ 0 & A_{3,2} & A_{3,3} & A_{3,4} & A_{3,5} & 0 & A_{3,7} & 0 & A_{3,9} & 0 & A_{3,11} \\ 0 & 0 & 0 & 1 & 0 & 0 & 0 & 0 & 0 & 0 & 0 \\ 0 & A_{5,2} & A_{5,3} & 0 & A_{5,5} & A_{5,6} & A_{5,7} & 0 & 0 & 0 & 0 \\ 0 & 0 & 0 & 0 & 0 & 1 & 0 & 0 & 0 & 0 & 0 \\ A_{7,1} & A_{7,2} & A_{7,3} & A_{7,4} & 0 & A_{7,6} & 0 & A_{7,8} & 0 & A_{7,10} & 0 \\ 0 & 0 & 0 & 0 & 0 & 0 & 0 & 0 & 1 & 0 & 0 \\ 0 & 0 & A_{9,3} & 0 & 0 & 0 & 0 & A_{9,8} & A_{9,9} & A_{9,10} & 0 \\ 0 & 0 & 0 & 0 & 0 & 0 & 0 & 0 & 0 & 0 & 1 \\ 0 & 0 & A_{11,3} & 0 & 0 & 0 & 0 & A_{11,8} & 0 & A_{11,10} & A_{11,11} \end{bmatrix} \quad (\text{A } 1)$$

and the matrix components are

$$A_{1,3} = -\mathcal{F}_\rho \left(\frac{1}{r} + \frac{d}{dr} \right) - \frac{\partial \mathcal{F}_\rho}{\partial Z} \frac{d\bar{Z}}{dr} - \frac{\partial \mathcal{F}_\rho}{\partial C} \frac{d\bar{C}}{dr}, \quad A_{1,5} = -i \frac{m \mathcal{F}_\rho}{r}, \quad (\text{A } 2)$$

$$A_{1,8} = i\omega \frac{\partial \mathcal{F}_\rho}{\partial Z}, \quad A_{1,10} = i\omega \frac{\partial \mathcal{F}_\rho}{\partial C}, \quad (\text{A } 3)$$

$$A_{3,2} = \frac{1}{3} \frac{1}{Re} \mathcal{F}_\mu \frac{d}{dr} - \frac{2}{3} \frac{1}{Re} \left(\frac{\partial \mathcal{F}_\mu}{\partial C} \frac{d\bar{C}}{dr} + \frac{\partial \mathcal{F}_\mu}{\partial Z} \frac{d\bar{Z}}{dr} \right), \quad (\text{A } 4)$$

$$A_{3,3} = i\omega \mathcal{F}_\rho - \frac{1}{Re} \frac{\mathcal{F}_\mu}{r^2} \left(m^2 + \frac{4}{3} \right) - \frac{2}{3} \frac{1}{Re r} \left(\frac{\partial \mathcal{F}_\mu}{\partial Z} \frac{d\bar{Z}}{dr} + \frac{\partial \mathcal{F}_\mu}{\partial C} \frac{d\bar{C}}{dr} - 2\mathcal{F}_\mu \frac{d}{dr} \right) + \frac{4}{3} \frac{1}{Re} \left(\frac{\partial \mathcal{F}_\mu}{\partial Z} \frac{d\bar{Z}}{dr} \frac{d}{dr} + \frac{\partial \mathcal{F}_\mu}{\partial C} \frac{d\bar{C}}{dr} \frac{d}{dr} + \mathcal{F}_\mu \frac{d^2}{dr^2} \right), \quad (\text{A } 5)$$

$$A_{3,4} = -\mathcal{F}_\rho \bar{u}, \quad A_{3,5} = -i \frac{2}{3} \frac{m}{Re r} \left(\frac{\partial \mathcal{F}_\mu}{\partial Z} \frac{\partial \bar{Z}}{\partial r} + \frac{\partial \mathcal{F}_\mu}{\partial C} \frac{\partial \bar{C}}{\partial r} - \frac{\mathcal{F}_\mu}{2} \frac{d}{dr} + \frac{7}{2} \frac{\mathcal{F}_\mu}{r} \right), \quad (\text{A } 6)$$

$$A_{3,7} = -\frac{d}{dr}, \quad A_{3,9} = \frac{1}{Re} \frac{d\bar{u}}{dr} \frac{\partial \mathcal{F}_\mu}{\partial Z}, \quad (\text{A } 7)$$

$$A_{3,11} = \frac{1}{Re} \frac{d\bar{u}}{dr} \frac{\partial \mathcal{F}_\mu}{\partial C}, \quad (\text{A } 8)$$

$$A_{5,2} = i \frac{1}{3} \frac{m \mathcal{F}_\mu}{Re r}, \quad A_{5,3} = i \frac{m}{Re r} \left(\frac{\mathcal{F}_\mu}{3} \frac{d}{dr} + \frac{\mathcal{F}_\mu}{\partial Z} \frac{d\bar{Z}}{dr} + \frac{\mathcal{F}_\mu}{\partial C} \frac{d\bar{C}}{dr} + \frac{7}{3} \frac{\mathcal{F}_\mu}{r} \right), \quad (\text{A } 9)$$

$$A_{5,5} = i\omega \mathcal{F}_\rho - \frac{\mathcal{F}_\mu}{Re} \left(\frac{1}{r^2} - \frac{1}{r} \frac{d}{dr} - \frac{d^2}{dr^2} + \frac{4}{3} \frac{m^2}{r^2} \right) + \frac{1}{Re} \left(\frac{\partial \mathcal{F}_\mu}{\partial Z} \frac{d\bar{Z}}{dr} + \frac{\partial \mathcal{F}_\mu}{\partial C} \frac{d\bar{C}}{dr} \right) \frac{d}{dr} - \frac{1}{Re r} \left(\frac{\partial \mathcal{F}_\mu}{\partial Z} \frac{d\bar{Z}}{dr} + \frac{\partial \mathcal{F}_\mu}{\partial C} \frac{d\bar{C}}{dr} \right), \quad (\text{A } 10)$$

$$A_{5,6} = -\mathcal{F}_\rho \bar{u}, \quad A_{5,7} = -i \frac{m}{r}, \quad (\text{A } 11)$$

$$A_{7,1} = i\omega \mathcal{F}_\rho + \frac{\mathcal{F}_\mu}{Re} \left(\frac{d^2}{dr^2} - \frac{m^2}{r^2} + \frac{1}{r} \frac{d}{dr} \right) + \frac{1}{Re} \left(\frac{\partial \mathcal{F}_\mu}{\partial Z} \frac{d\bar{Z}}{dr} + \frac{\partial \mathcal{F}_\mu}{\partial C} \frac{d\bar{C}}{dr} \right) \frac{d}{dr}, \quad (\text{A } 12)$$

$$A_{7,2} = -\mathcal{F}_\rho \bar{u}, \quad A_{7,3} = -\mathcal{F}_\rho \frac{d\bar{u}}{dr}, \quad (\text{A } 13)$$

$$A_{7,4} = \frac{1}{3} \frac{\mathcal{F}_\mu}{Re} \left(\frac{1}{r} + \frac{d}{dr} \right) + \frac{1}{Re} \left(\frac{\partial \mathcal{F}_\mu}{\partial Z} \frac{d\bar{Z}}{dr} + \frac{\partial \mathcal{F}_\mu}{\partial C} \frac{d\bar{C}}{dr} \right), \quad A_{7,6} = i \frac{1}{3} \frac{\mathcal{F}_\mu}{Re} \frac{m}{r}, \quad (\text{A } 14)$$

$$A_{7,8} = \frac{1}{Re} \frac{\partial \mathcal{F}_\mu}{\partial Z} \left(\frac{d\bar{u}}{dr} \frac{d}{dr} + \frac{d^2 \bar{u}}{dr^2} + \frac{1}{r} \frac{d\bar{u}}{dr} \right) + \frac{1}{Re} \frac{d\bar{u}}{dr} \left(\frac{\partial^2 \mathcal{F}_\mu}{\partial Z^2} \frac{d\bar{Z}}{dr} + \frac{\partial^2 \mathcal{F}_\mu}{\partial Z \partial C} \frac{d\bar{C}}{dr} \right) - \frac{1}{Fr^2} \frac{\partial \mathcal{F}_\rho}{\partial Z}, \quad (\text{A } 15)$$

$$A_{7,10} = \frac{1}{Re} \frac{\partial \mathcal{F}_\mu}{\partial C} \left(\frac{d\bar{u}}{dr} \frac{d}{dr} + \frac{d^2 \bar{u}}{dr^2} + \frac{1}{r} \frac{d\bar{u}}{dr} \right) + \frac{1}{Re} \frac{d\bar{u}}{dr} \left(\frac{\partial^2 \mathcal{F}_\mu}{\partial Z \partial C} \frac{d\bar{Z}}{dr} + \frac{\partial^2 \mathcal{F}_\mu}{\partial C^2} \frac{d\bar{C}}{dr} \right) - \frac{1}{Fr^2} \frac{\partial \mathcal{F}_\rho}{\partial C}, \quad (\text{A } 16)$$

$$A_{9,3} = -\mathcal{F}_\rho \frac{d\bar{Z}}{dr}, \quad (\text{A } 17)$$

$$A_{9,8} = i\omega \mathcal{F}_\rho + \frac{\mathcal{F}_v}{Re Sc} \left(\frac{1}{r} \frac{d}{dr} + \frac{d^2}{dr^2} - \frac{m^2}{r^2} \right) + \frac{1}{Re Sc} \frac{\partial \mathcal{F}_v}{\partial Z} \left(\frac{1}{r} \frac{d\bar{Z}}{dr} + 2 \frac{d\bar{Z}}{dr} \frac{d}{dr} + \frac{d^2 \bar{Z}}{dr^2} \right) + \frac{1}{Re Sc} \left(\frac{\partial^2 \mathcal{F}_v}{\partial Z^2} \left(\frac{d\bar{Z}}{dr} \right)^2 + \frac{\partial^2 \mathcal{F}_v}{\partial Z \partial C} \frac{d\bar{Z}}{dr} \frac{d\bar{C}}{dr} \right) + \frac{1}{Re Sc} \frac{\partial \mathcal{F}_v}{\partial C} \frac{d\bar{C}}{dr} \frac{d}{dr}, \quad (\text{A } 18)$$

$$A_{9,9} = -\mathcal{F}_\rho \bar{u}, \quad (\text{A } 19)$$

$$A_{9,10} = \frac{1}{Re Sc} \frac{\partial \mathcal{F}_v}{\partial C} \left(\frac{1}{r} \frac{d\bar{Z}}{dr} + \frac{d\bar{Z}}{dr} \frac{d}{dr} + \frac{d^2 \bar{Z}}{dr^2} \right) + \frac{1}{Re Sc} \left(\frac{\partial^2 \mathcal{F}_v}{\partial Z \partial C} \left(\frac{d\bar{Z}}{dr} \right)^2 + \frac{\partial^2 \mathcal{F}_v}{\partial C^2} \frac{d\bar{Z}}{dr} \frac{d\bar{C}}{dr} \right), \quad (\text{A } 20)$$

$$A_{11,3} = -\mathcal{F}_\rho \frac{d\bar{C}}{dr}, \quad (\text{A } 21)$$

$$A_{11,8} = \frac{1}{Re Sc} \frac{\partial \mathcal{F}_v}{\partial Z} \left(\frac{1}{r} \frac{d\bar{C}}{dr} + \frac{d\bar{C}}{dr} \frac{d}{dr} + \frac{d^2 \bar{C}}{dr^2} \right) + \frac{1}{Re Sc} \left(\frac{\partial^2 \mathcal{F}_v}{\partial Z^2} \frac{d\bar{Z}}{dr} \frac{d\bar{C}}{dr} + \frac{\partial^2 \mathcal{F}_v}{\partial Z \partial C} \left(\frac{d\bar{C}}{dr} \right)^2 \right) + \frac{\partial \mathcal{F}_{\dot{\omega}_c}}{\partial Z}, \quad (\text{A } 22)$$

$$A_{11,10} = i\omega \mathcal{F}_\rho + \frac{\mathcal{F}_v}{Re Sc} \left(\frac{1}{r} \frac{d}{dr} + \frac{d^2}{dr^2} - \frac{m^2}{r^2} \right) + \frac{1}{Re Sc} \frac{\partial \mathcal{F}_v}{\partial C} \left(\frac{1}{r} \frac{d\bar{C}}{dr} + 2 \frac{d\bar{C}}{dr} \frac{d}{dr} + \frac{d^2 \bar{C}}{dr^2} \right) + \frac{1}{Re Sc} \left(\frac{\partial^2 \mathcal{F}_v}{\partial C^2} \left(\frac{d\bar{C}}{dr} \right)^2 + \frac{\partial^2 \mathcal{F}_v}{\partial Z \partial C} \frac{d\bar{Z}}{dr} \frac{d\bar{C}}{dr} \right) + \frac{1}{Re Sc} \frac{\partial \mathcal{F}_v}{\partial Z} \frac{d\bar{Z}}{dr} \frac{d}{dr} + \frac{\partial \mathcal{F}_{\dot{\omega}_c}}{\partial C}, \quad (\text{A } 23)$$

$$A_{11,10} = -\mathcal{F}_\rho \bar{u}. \quad (\text{A } 24)$$

The matrix \mathbf{B} on the right-hand side of (2.11) is sparse and can be written as

$$\mathbf{B} = \begin{bmatrix} B_{1,1} & 0 & 0 & 0 & 0 & 0 & 0 & B_{1,8} & 0 & B_{1,10} & 0 \\ 1 & 0 & 0 & 0 & 0 & 0 & 0 & 0 & 0 & 0 & 0 \\ 0 & 0 & 0 & B_{3,4} & 0 & 0 & 0 & 0 & 0 & 0 & 0 \\ 0 & 0 & 1 & 0 & 0 & 0 & 0 & 0 & 0 & 0 & 0 \\ 0 & 0 & 0 & 0 & 0 & B_{5,6} & 0 & 0 & 0 & 0 & 0 \\ 0 & 0 & 0 & 0 & 1 & 0 & 0 & 0 & 0 & 0 & 0 \\ 0 & B_{7,2} & 0 & 0 & 0 & 0 & 1 & 0 & 0 & 0 & 0 \\ 0 & 0 & 0 & 0 & 0 & 0 & 0 & 1 & 0 & 0 & 0 \\ 0 & 0 & 0 & 0 & 0 & 0 & 0 & 0 & 0 & B_{9,9} & 0 \\ 0 & 0 & 0 & 0 & 0 & 0 & 0 & 0 & 0 & 1 & 0 \\ 0 & 0 & 0 & 0 & 0 & 0 & 0 & 0 & 0 & 0 & B_{11,11} \end{bmatrix} \quad (\text{A 25})$$

and the corresponding matrix elements are

$$B_{1,1} = \mathcal{F}_\rho, \quad B_{1,8} = \bar{u} \frac{\partial \mathcal{F}_\rho}{\partial Z}, \quad B_{1,10} = \bar{u} \frac{\partial \mathcal{F}_\rho}{\partial C}, \quad (\text{A 26})$$

$$B_{3,4} = -\frac{\mathcal{F}_\mu}{Re}, \quad (\text{A 27})$$

$$B_{5,6} = -\frac{\mathcal{F}_\mu}{Re}, \quad (\text{A 28})$$

$$B_{7,2} = -\frac{4 \mathcal{F}_\mu}{3 Re}, \quad (\text{A 29})$$

$$B_{9,9} = -\frac{\mathcal{F}_v}{Re Sc}, \quad (\text{A 30})$$

$$B_{11,11} = -\frac{\mathcal{F}_v}{Re Sc}. \quad (\text{A 31})$$

Appendix B. Evaluation of growth rate and phase speed from simulations

Following (2.10), the global instability mode of an axisymmetric perturbation ($m=0$) in a weakly non-parallel mean flow can be represented as

$$\phi' = \operatorname{Re} \left(\hat{\phi}(r; x) \exp \left\{ i \left(\int_0^x \alpha(\xi) d\xi - \omega t \right) \right\} \right), \quad (\text{B 1})$$

where $\hat{\phi}(x; r)$ is the normalized instability mode, which has been phase-aligned at $r=r_0$. By denoting the axisymmetric unsteady component of the detailed simulation as $\varphi'(r, x, t)$ and the corresponding Fourier-transformed solution as $\hat{\varphi}(r, x, \omega_r)$, explicit expressions for the real and imaginary parts of the axial wavenumber can be derived. For this, we equate the Fourier mode at the forcing frequency ω_r from the simulation with that of the stability analysis:

$$\operatorname{Re}(\bar{\varphi}(r, x, \omega_r) \exp\{-i\omega_r t\}) = \operatorname{Re} \left(\hat{\phi}(r; x) \exp \left\{ i \int_0^x \alpha(\xi) d\xi \right\} \exp\{-i\omega_r t\} \right). \quad (\text{B 2})$$

Then, a comparison of coefficients yields

$$\bar{\varphi}(r, x, \omega_r) = \hat{\phi}(r; x) \exp \left\{ i \int_0^x \alpha(\xi) d\xi \right\}. \quad (\text{B 3})$$

Written in polar form, this equation can be evaluated at the radial location of the phase alignment $r = r_0$, resulting in the following expression:

$$\begin{aligned} & |\bar{\phi}(r_0, x, \omega_r)| \exp\{i \arg(\bar{\phi}(r_0, x, \omega_r))\} \\ &= |\hat{\phi}(r_0; x)| \exp\left\{-\int_0^x \alpha_i(\xi) d\xi\right\} \exp\left\{i\left(\int_0^x \alpha_r(\xi) d\xi + \arg(\hat{\phi}(r_0))\right)\right\}. \end{aligned} \quad (\text{B } 4)$$

Note that by phase-aligning the instability mode, the argument of $\hat{\phi}$ becomes independent of x . The real part of the wavenumber, α_r , can then be evaluated by differentiating the complex-valued arguments with respect to x :

$$\alpha_r(x) = \frac{d}{dr} \arg(\bar{\phi}(r_0, x, \omega_r)), \quad (\text{B } 5)$$

from which the phase speed can be evaluated via (4.3).

The growth rate is obtained by multiplying (B 3) and integrating in the radial direction, to give

$$\{\hat{\phi}, \bar{\phi}\} = \exp\left\{-2 \int_0^x \alpha_i(\xi) d\xi\right\}, \quad (\text{B } 6)$$

where $\{\hat{\phi}, \bar{\phi}\} \equiv \int_0^\infty \hat{\phi}(r, x, \omega_r) \bar{\phi}(r, x, \omega_r) r dr$. The growth rate is then evaluated by differentiating:

$$a_i(x) = -\frac{1}{2\{\hat{\phi}, \bar{\phi}\}} \frac{d\{\hat{\phi}, \bar{\phi}\}}{dx}. \quad (\text{B } 7)$$

Equations (B 5) and (B 7) are used to evaluate the wavelength and growth rate from the detailed simulation results.

REFERENCES

- BECKER, H. A. & YAMAZAKI, S. 1978 Entrainment, momentum flux and temperature in vertical free turbulent diffusion flames. *Combust. Flame* **33** (2), 123–149.
- BERGMANN, M., BRUNEAU, C.-H. & IOLLO, A. 2009 Enablers for robust POD models. *J. Comput. Phys.* **228**, 516–538.
- BIRD, R. B., STEWART, W. E. & LIGHTFOOT, E. N. 2007 *Transport Phenomena*. rev. 2nd edn. John Wiley & Sons.
- BOWMAN, C. T., HANSON, R. K., DAVIDSON, D. F., GARDINER, W. C., LISSIANSKI, V., SMITH, G. P., GOLDEN, D. M., FRENKLACH, M. & GOLDENBERG, M. 1997 GRI-Mech 2.11. Available at: <http://www.me.berkeley.edu/gri-mech/>.
- BRIGGS, R. J. 1964 *Electron-Stream Interaction with Plasmas*. MIT Press.
- BUCKMASTER, J. & PETERS, N. 1988 The infinite candle and its stability—a paradigm for flickering diffusion flames. *Proc. Combust. Inst.* **21** (1), 1829–1836.
- CHAMBERLIN, D. S. & ROSE, A. 1948 The flicker of luminous flames. *Proc. Combust. Inst.* **1–2**, 27–32.
- CHEN, L.-D., SEABA, J. P., ROQUEMORE, W. M. & GOSS, L. P. 1989 Buoyant diffusion flames. *Proc. Combust. Inst.* **22** (1), 677–684.
- CHOMAZ, J.-M. 2005 Global instabilities in spatially developing flows: non-normality and nonlinearity. *Annu. Rev. Fluid Mech.* **37** (1), 357–392.

- CHOMAZ, J. M., HUERRE, P. & REDEKOPP, L. G. 1988 Bifurcations to local and global modes in spatially developing flows. *Phys. Rev. Lett.* **60** (1), 25–28.
- COENEN, W. & SEVILLA, A. 2012 The structure of the absolutely unstable regions in the near field of low-density jets. *J. Fluid Mech.* **713**, 123–149.
- COENEN, W., SEVILLA, A. & SÁNCHEZ, A. L. 2008 Absolute instability of light jets emerging from circular injector tubes. *Phys. Fluids* **20**, 074104.
- CRIGHTON, D. G., DOWLING, A. P., FLOWCS WILLIAMS, J. E., HECKL, M. & LEPPINGTON, F. G. 1992 *Modern Methods in Analytical Acoustics: Lecture Notes*. Springer.
- CRIGHTON, D. G. & GASTER, M. 1976 Stability of slowly diverging jet flow. *J. Fluid Mech.* **77**, 397–413.
- DAY, M. J., REYNOLDS, W. C. & MANSOUR, N. N. 1998 The structure of the compressible reacting mixing layer: insights from linear stability analysis. *Phys. Fluids* **10** (4), 993–1007.
- FÜRI, M. 2001 Non-premixed jet flame instabilities. Thèse No. 2468 (2001), École Polytechnique Fédérale de Lausanne.
- FÜRI, M., PAPAS, P. & MONKEWITZ, P. A. 2000 Non-premixed jet flame pulsations near extinction. *Proc. Combust. Inst.* **28**, 831–838.
- FÜRI, M., PAPAS, P., RAIS, R. M. & MONKEWITZ, P. A. 2002 The effect of flame position on the Kelvin–Helmholtz instability in non-premixed jet flames. *Proc. Combust. Inst.* **29**, 1653–1661.
- HAN, D. & MUNGAL, M. G. 2001 Direct measurement of entrainment in reacting/non-reacting turbulent jets. *Combust. Flame* **124** (3), 370–386.
- HIRSCHFELDER, J. O. & CURTISS, C. F. 1949 Theory of propagation of flames. Part I: General equations. *Symp. Combust. Flame Explos. Phenom.* **3** (1), 121–127.
- HOLMES, P., LUMLEY, J. L. & BERKOOZ, G. 1998 *Turbulence, Coherent Structures, Dynamical Systems, and Symmetry*. Cambridge University Press.
- HUERRE, P. & MONKEWITZ, P. A. 1990 Local and global instabilities in spatially developing flows. *Annu. Rev. Fluid Mech.* **22**, 473–537.
- IHME, M., CHA, C. M. & PITSCHE, H. 2005 Prediction of local extinction and re-ignition effects in non-premixed turbulent combustion using a flamelet/progress variable approach. *Proc. Combust. Inst.* **30**, 793–800.
- IHME, M., SHUNN, L. & ZHANG, J. 2012 Regularization of reaction progress variable for application to flamelet-based combustion models. *J. Comput. Phys.* **231** (23), 7715–7721.
- JUNIPER, M. P., LI, L. K. B. & NICHOLS, J. W. 2009 Forcing of self-excited round jet diffusion flames. *Proc. Combust. Inst.* **32**, 1191–1198.
- KATTA, V. R., GOSS, L. P. & ROQUEMORE, W. M. 1994 Effect of non-unity Lewis number and finite-rate chemistry on the dynamics of a hydrogen–air jet diffusion flame. *Combust. Flame* **96**, 60–74.
- KATTA, V. R. & ROQUEMORE, W. M. 1993 Role of inner and outer structures in transitional jet diffusion flame. *Combust. Flame* **92**, 274–282.
- KORTSCHIK, C., HONNET, S. & PETERS, N. 2005 Influence of curvature on the onset of autoignition in a corrugated counterflow mixing field. *Combust. Flame* **114**, 140–152.
- KREISS, H.-O., LORENZ, J. & NAUGHTON, M. J. 1991 Convergence of the solutions of the compressible to the solutions of the incompressible Navier–Stokes equations. *Adv. Appl. Math.* **12**, 187–214.
- KURDYUMOV, V. N. & MATALON, M. 2002 Radiation losses as a driving mechanism for flame oscillations. *Proc. Combust. Inst.* **29**, 45–52.
- LEE, D. J., THAKUR, S., WRIGHT, J., IHME, M. & SHYY, W. 2011 Characterization of flow field structure and species composition in a shear coaxial rocket GH2/GO2 injector: modeling of wall heat losses. *AIAA Paper* 2011-6125.
- LESSHAFT, L. & MARQUET, O. 2010 Optimal velocity and density profiles for the onset of absolute instability in jets. *J. Fluid Mech.* **662**, 398–408.
- LINGENS, A., NEEMANN, K., MEYER, J. & SCHREIBER, M. 1996 Instability of diffusion flames. *Proc. Combust. Inst.* **26** (1), 1053–1061.
- LO JACONO, D. & MONKEWITZ, P. A. 2007 Scaling of cell size in cellular instabilities of non-premixed jet flames. *Combust. Flame* **151**, 321–332.

- MATALON, M. 2007 Intrinsic flame instabilities in premixed and non-premixed combustion. *Annu. Rev. Fluid Mech.* **39**, 163–191.
- MAXWORTHY, T. 1999 The flickering candle: transition to a global oscillation in a thermal plume. *J. Fluid Mech.* **390**, 297–323.
- MCBRIDE, B. J., ZEHE, M. J. & GORDON, S. 2002 NASA Glenn coefficients for calculating thermodynamic properties of individual species. *NASA/TP Rep.* 2002-211556. NASA.
- MICHALKE, A. 1984 Survey on jet instability theory. *Prog. Aerosp. Sci.* **21**, 159–199.
- MONKEWITZ, P. A. & SOHN, K. D. 1988 Absolute instability in hot jets. *AIAA J.* **26** (8), 911–916.
- MÜLLER, B. 1999 Low Mach number asymptotics of the Navier–Stokes equations and numerical implications. In *Proc. 30th Computational Fluid Dynamics Lecture Series*. Von Karman Institute for Fluid Dynamics.
- MUÑIZ, L. & MUNGAL, M. G. 2001 Effects of heat release and buoyancy on flow structure and entrainment in turbulent non-premixed flames. *Combust. Flame* **126** (1–2), 1402–1420.
- NAYFEH, A. H. 2000 *Perturbation Methods*. Wiley-VCH.
- NICHOLS, J. W. & SCHMID, P. J. 2008 The effect of a lifted flame on the stability of round fuel jets. *J. Fluid Mech.* **609**, 275–284.
- NICHOLS, J. W., SCHMID, P. J. & RILEY, J. J. 2007 Self-sustained oscillations in variable-density round jets. *J. Fluid Mech.* **582**, 341–376.
- OBERLEITHNER, K., SIEBER, M., NAYERI, C. N., PASCHEREIT, C. O., PETZ, C., HEGE, H.-C., NOACK, B. R. & WYGNANSKI, I. 2011 Three-dimensional coherent structures in a swirling jet undergoing vortex breakdown: stability analysis and empirical mode construction. *J. Fluid Mech.* **679**, 383–414.
- PAPAS, P., RAIS, R. M., MONKEWITZ, P. A. & TOMBOULIDES, A. G. 2003 Instabilities of diffusion flames near extinction. *Combust. Theory. Model.* **7**, 603–633.
- PETERS, N. 1983 Local quenching due to flame stretch and non-premixed turbulent combustion. *Combust. Sci. Technol.* **30**, 1–17.
- PETERS, N. 1984 Laminar diffusion flamelet models in non-premixed turbulent combustion. *Prog. Energy Combust. Sci.* **10** (3), 319–339.
- PIER, B. & HUERRE, P. 2001 Nonlinear self-sustained structures and fronts in spatially developing wake flows. *J. Fluid Mech.* **435**, 145–174.
- PIERCE, C. D. & MOIN, P. 2004 Progress-variable approach for large-eddy simulation of non-premixed turbulent combustion. *J. Fluid Mech.* **504**, 73–97.
- PITSCH, H. & PETERS, N. 1998 A consistent flamelet formulation for non-premixed combustion considering differential diffusion effects. *Combust. Flame* **114** (1–2), 26–40.
- SCHMID, P. J. & HENNINGSON, D. S. 2001 *Stability and Transition in Shear Flows*. Applied Mathematical Sciences. vol. 142. Springer.
- SHIN, D. S. & FERZIGER, J. H. 1991 Linear stability of the reacting mixing layer. *AIAA J.* **29** (10), 1634–1642.
- SIROVICH, L. 1987 Turbulence and the dynamics of coherent structures. 1. Coherent structures. *Q. Appl. Maths* **45**, 561–571.
- SRINIVASAN, V., HALLBERG, M. P. & STRYKOWSKI, P. J. 2010 Viscous linear stability of axisymmetric low-density jets: parameters influencing absolute instability. *Phys. Fluids* **22**, 024103.
- THEOFILIS, V. 2011 Global linear instability. *Annu. Rev. Fluid Mech.* **43**, 319–352.
- WESTBROOK, C. K. & DRYER, F. L. 1981 Simplified reaction mechanisms for the oxidation of hydrocarbon fuels in flames. *Combust. Sci. Technol.* **27**, 31–43.
- WILKE, C. R. 1950 A viscosity equation for gas mixtures. *J. Chem. Phys.* **18** (4), 517–519.
- WILLIAMS, F. A. 1991 Overview of asymptotics for methane flames. In *Reduced Kinetic Mechanisms and Asymptotic Approximations for Methane–Air Flames* (ed. M. D. Smooke), pp. 68–85. Springer.